

Effects of ambient fluids on particle size segregation in saturated debris flows

Gordon G. D. Zhou¹, Kahlil Fredrick Ermac Cui², Lu Jing³, Tao Zhao⁴, Dongri Song², and Yu Huang⁵

¹Institute of Mountain Hazards and Environment

²Institute of Mountain Hazards and Environment, Chinese Academy of Sciences

³The University of Hong Kong

⁴Brunel University

⁵Department of Geotechnical Engineering, College of Civil Engineering, Tongji University

November 21, 2022

Abstract

Size segregation, which is a robust feature of sheared granular mixtures and geophysical mass flow deposits, is found to diminish in the presence of a viscous fluid. We study this inhibitive effect through coupled fluid-particle simulations of fully saturated granular flows. Granular-fluid mixture flows are modelled according to three distinct flow regimes – free-fall, fluid-inertial, and viscous – at different angles of inclination. Each flow regime corresponds to distinct flow dynamics and segregation behaviors. We find that segregation is indeed weaker and slower in the presence of an ambient fluid which is more so as the flow becomes more viscous. The ambient fluid affects segregation in two major ways. Firstly, buoyancy reduces the contact pressure gradients which are needed to drive large particles up, which at the same time reduces the particles' apparent weight. On the other hand, the streamwise drag force substantially changes the flow rheology, specifically the shear rate profile, thereby modifying the segregation behavior in the normal direction. Surprisingly, the fluid drag in the normal direction is negligible regardless of the fluid viscosity and does not affect segregation in a direct manner.

Effects of ambient fluids on particle size segregation in saturated debris flows

Gordon G.D. Zhou^{1,2}, Kahlil F.E. Cui^{1,2}, Lu Jing^{3,4}, Tao Zhao^{1,5}, Dongri Song^{1,2}, Yu Huang⁶

¹ Key Laboratory of Mountain Hazards and Earth Surface Process, Chinese Academy of Sciences, Chengdu 61000, China

² Institute of Mountain Hazards and Environment, Chinese Academy of Sciences & Ministry of Water Conservancy, Chengdu 61000, China

³ Department of Chemical and Biological Engineering, Northwestern University, Evanston, IL 60208, USA

⁴ Department of Civil Engineering, The University of Hong Kong, Pokfulam Road, Hong Kong, China

⁵ Department of Civil and Environmental Engineering, Brunel University London, London, UB8 3PH, United Kingdom

⁶ Department of Geotechnical Engineering, College of Civil Engineering, Tongji University, Shanghai 200092, China

Corresponding author: Kahlil Fredrick Cui (kfcui@imde.ac.cn)

Key Points:

- Coupled fluid-particle simulations show that a viscous ambient fluid slows down size segregation.
- Ambient fluid affects segregation by reducing particle contact forces and through drag force-induced modification of shear rate profiles.
- Segregation velocities in different flow regimes follow a similar scaling if fluid effects are appropriately considered.

27 Abstract

28 Size segregation, which is a robust feature of sheared granular mixtures and geophysical mass
29 flow deposits, is found to diminish in the presence of a viscous fluid. We study this inhibitive
30 effect through coupled fluid-particle simulations of fully saturated granular flows. Granular-fluid
31 mixture flows are modelled according to three distinct flow regimes – free-fall, fluid-inertial, and
32 viscous – at different angles of inclination. Each flow regime corresponds to distinct flow
33 dynamics and segregation behaviors. We find that segregation is indeed weaker and slower in the
34 presence of an ambient fluid which is more so as the flow becomes more viscous. The ambient
35 fluid affects segregation in two major ways. Firstly, buoyancy reduces the contact pressure
36 gradients which are needed to drive large particles up, which at the same time reduces the
37 particles' apparent weight. On the other hand, the streamwise drag force substantially changes
38 the flow rheology, specifically the shear rate profile, thereby modifying the segregation behavior
39 in the normal direction. Surprisingly, the fluid drag in the normal direction is negligible
40 regardless of the fluid viscosity and does not affect segregation in a direct manner.

41 **Key words:** Size segregation, flow regimes, saturated granular flows, CFD-DEM

42 1 Introduction

43 Granular flows comprising particles of different sizes (Savage & Lun, 1988), shapes
44 (Zhao et al., 2018; Mandal & Khakhar, 2019), and densities (Tripathi & Khakhar, 2013;
45 Tunuguntla et al., 2014) have a tendency to segregate according to these species properties.
46 Understanding and predicting segregation is relevant to processes where separation of different
47 species may be either desired or avoided (Fan et al., 2014). Particle size segregation, with or
48 without the presence of a viscous fluid, is of particular importance to geophysical flows, such as

49 debris flows and landslides (Johnson et al., 2012; de Haas et al., 2015), as it consequently leads
50 to formation of run-out enhancing features such as flow-lubricating basal layers (Linares-
51 Guerrero et al., 2007; Lai et al., 2017), channelizing levees (Johnson et al., 2012; Kokelaar et al.,
52 2014; Baker et al., 2016), and coarse particle-rich heads (Gray & Ancey, 2009; Zhou & Ng,
53 2010; van der Vaart et al., 2018). Particle size segregation is also a significant process in
54 riverbed armoring (Ferdowsi et al., 2017), grain sorting on the lee side of dunes (Kleinhans,
55 2004), and layer formation in faults (Siman-Tov & Brodsky, 2018; Itoh & Hatano, 2019).

56 Shear-induced size segregation in granular flows can be explained by the theory of
57 kinetic sieving (Savage & Lun 1988; Vallance & Savage 2000), whereby small particles
58 preferentially fall down into randomly generated voids beneath them while large particles are
59 rolled up (Jing et al., 2017) to the free surface due to unbalanced contact forces (Gray &
60 Thornton, 2005; Staron & Phillips, 2015). The downward percolation of small particles is
61 stepwise, travelling down one layer at a time while sustaining minimal enduring contacts, as it
62 makes its way through voids to the bed (van der Vaart et al., 2015; Jing et al. 2017). Large
63 particles migrate upward “smoothly”, relying on the rearrangement and persistent contacts of the
64 smaller particles around them (Jing et al., 2017). The fluctuating forces acting on large particles,
65 when coupled with the local shear, can effectively push them up (Guillard et al., 2016; Jing et al.,
66 2017; Staron, 2018). In addition to – or instead of – kinetic sieving is the percolation driven by
67 kinetic stress gradients (i.e. velocity fluctuations, analogous to granular temperature) (Fan &
68 Hill, 2011b; Hill & Tan, 2014) whereby large particles are segregated to regions of low kinetic
69 stress (i.e. free-surface) (Dahl & Hrenya, 2004). Competing with the upward and downward
70 percolation is the diffusive remixing which results from random collisions and shearing of

71 particles over each other (Gray & Chugunov, 2006). Diffusive remixing becomes more
72 significant in rapid flows where it results in a more diffuse and poorly-graded mixture.

73 In dry granular flows, the aforementioned micro-mechanisms result in inversely-graded
74 granular layers separated by a sharp concentration jump, the sharpness of which is determined by
75 the relative intensity of percolation and diffusive remixing. These processes are determined
76 under the assumption that the interstitial fluid is negligible. However, real-world granular flows
77 are water-laden (i.e. debris flows and mud flows) or are completely submerged (i.e. submarine
78 landslides and sediment flows), where solid-fluid interactions become significant and actively
79 influence the particle dynamics and subsequent re-arrangement (Coussot & Meunier, 1996;
80 Iverson, 1997). In such cases, segregation is not as evident or is completely absent depending on
81 various factors such as saturation (Major & Pierson, 1992; Zhou et al., 2019), grain-size
82 distribution (Zanuttigh & Ghilardi, 2010), and fluid properties (Vallance & Savage, 2000).
83 Although dry granular segregation has already been extensively studied, the role of fluids in this
84 process remains unclear. Through chute flow experiments of bi-disperse granular-fluid mixtures,
85 Vallance and Savage (2000) found that segregation in these cases is not as dramatic as dry flows
86 – the grading is more diffuse – indicating that the presence of fluids inhibits segregation. They
87 further concluded that segregation is weaker in water than it is in a more viscous yet less dense
88 fluid, which implies that the resulting inhibition depends on the relative densities of the particles
89 and the fluid phases rather than on the fluid viscosity. This was later confirmed by Thornton et
90 al. (2006) in which they derived, theoretically, that the percolation velocity decreases as the fluid
91 density approaches that of the particles and increases as the fluid becomes negligible. Likewise,
92 the direction of percolation velocities reverses when the fluid becomes denser than the particles
93 and no segregation occurs when the mixture is neutrally buoyant. Zanuttigh and Ghilardi (2010)

94 investigated the dependence of granular-fluid segregation on the average grain size and
95 concluded that the increased presence of larger particles slows down segregation as it allows
96 more fluid between voids which then reduces collision among particles.

97 The recurring theme presented by the handful of research on segregation in granular-fluid
98 mixtures is that the role of interstitial or ambient fluid is simply to inhibit segregation. Although
99 intuitive, a fundamental understanding of the mechanical origin of this inhibitive effect is still
100 missing. In particular, it is interesting to study whether the presence of a fluid affects segregation
101 directly through buoyancy and drag, or indirectly by modifying the shear profile and flow
102 rheology. Evaluation of these fluid effects on the segregation process will enable better
103 prediction of grading patterns in granular-fluid mixtures and understanding of the driving
104 mechanisms responsible for particle re-arrangement in natural granular flows.

105 The primary aims of this research is to isolate and evaluate different fluid effects in
106 granular segregation when the ambient fluid is non-negligible. To this end, simplified
107 simulations are conducted using a coupled fluid-particle approach, where three-dimensional fully
108 saturated, steady granular flows down an incline are simulated. The modelled system is
109 analogous to a section of a fluid-saturated debris flow or avalanche containing both coarse and
110 fine particles. Although size segregation is likewise dependent on the size ratio and the volume
111 concentration distribution (Hill & Tan, 2014; Tunuguntla et al., 2014; Jing et al., 2017), only the
112 effect of the angle of inclination is explored as we focus on how the emerging rheology affects
113 segregation. In the subsequent sections, we first lay out the theoretical background and the
114 research methodology. We then present results relating to (i) the mixture flow rheology, (ii)
115 different forces acting on the segregating particles, and (iii) partitioning of contact and kinetic
116 stresses. We then discuss how the presence of an ambient fluid affects size segregation and how

117 these findings might be used to explain the level of inverse grading observed in natural mass
 118 flow deposits.

119 **2 Background**

120 2.1 Mixture theory and stress partitioning

121 Isolation of fluid effects can be achieved by evaluating the relative significance of
 122 different forcing terms in the momentum equations of the mixture theory of segregation, which
 123 deals with the evolution of partial variables defined per unit volume, with each partial variable
 124 defined for a specific phase in the mixture (Gray, 2018). A unit volume (i.e. volume element
 125 over which partial variables are calculated) is denoted as V_M , and a size bi-disperse mixture
 126 composed of large (L) and small (S) particles, with a passive interstitial pore fluid (F) (e.g. air,
 127 water) is considered. For convenience, we use an index $i = L, S$ to collectively represent the
 128 large- and small-particle phases, while $i' = L, S, F$ for all three phases. The fraction of volume
 129 occupied by a mixture component i' is the volume fraction $\Phi_{i'} = V_{i'}/V_M$, and the total volume
 130 fraction sums to unity (Thornton et al., 2006):

$$\sum_{i'} \Phi_{i'} = 1 \quad \text{where} \quad i' = L, S, F \quad (1)$$

131 The solid concentration ϕ_i is the ratio between the volume fraction of a particle size species Φ_i
 132 and the total granular volume fraction $\Phi = \Phi_L + \Phi_S$. The total solid concentration in a control
 133 volume also sums to unity, $\phi_L + \phi_S = 1$.

134 For a mixture of bi-disperse particles with a viscous interstitial fluid moving down an
 135 incline at a constant angle θ , in a coordinate system where the z -axis is pointing upward normal
 136 to the flow base, the x -axis along the direction of the flow, and the y -axis across the flow
 137 surface, the mass and momentum balances for each phase are given as:

$$\frac{\partial \Phi_{i'} \rho_{i'}}{\partial t} + \nabla \cdot (\Phi_{i'} \rho_{i'} \mathbf{U}_{i'}) = 0 \quad (2)$$

$$\frac{\partial}{\partial t} (\Phi_{i'} \rho_{i'} \mathbf{U}_{i'}) + \nabla \cdot (\Phi_{i'} \rho_{i'} \mathbf{U}_{i'} \otimes \mathbf{U}_{i'}) = -\nabla \cdot \boldsymbol{\sigma}_{i'} + \Phi_{i'} \rho_{i'} \mathbf{U}_{i'} + \beta \quad (3)$$

138 where $\boldsymbol{\sigma}_{i'} = \mathbf{1}P_{i'} + \mathbf{S}_{i'}$ is the Cauchy stress where $P_{i'}$ is the normal (called pressure for
 139 simplicity) and $\mathbf{S}_{i'}$ is the deviatoric component of the stress tensor. $\rho_{i'}$ is the phase material
 140 density and $\mathbf{U}_{i'} = (\mathbf{u}_{i'}, \mathbf{v}_{i'}, \mathbf{w}_{i'})$ is the partial velocity in three dimensions. The symbol \otimes
 141 represents a dyadic product, and $\mathbf{g} = (g \sin \theta, 0, -g \cos \theta)$ is the gravity vector where g is the
 142 acceleration due to gravity. It follows that the total density and total stress are defined as $\rho =$
 143 $\Phi_L \rho_L + \Phi_S \rho_S + \Phi_F \rho_F$ and $\boldsymbol{\sigma} = \boldsymbol{\sigma}_L + \boldsymbol{\sigma}_S + \boldsymbol{\sigma}_F$ respectively.

144 The third term on the right-hand side of the momentum equation is the force exerted by
 145 one of the constituent phases on the others. In a three-phase mixture, this term can be further
 146 broken down into forces exerted by one solid component on the other $\beta^{L \leftrightarrow S}$, and forces exerted
 147 by the solid and fluid phases on each other $\beta^{G \leftrightarrow F}$. The solid interaction force is analogous to the
 148 percolation of fluids through porous solids and commonly adopts the form motivated by Darcy's
 149 Law (Gray & Thornton, 2005; Gray & Chugunov, 2006;):

$$\beta^{L \leftrightarrow S} = -\Phi_i \rho_i c_{PI} (\mathbf{U}_i - \mathbf{U}) - \Phi \rho_G c_D \nabla \phi_i. \quad (4)$$

150 The first term in equation (4) expresses the relative velocity between the bulk and the individual
 151 phases where c_{PI} is the inter-phase drag coefficient. The final term represents diffusive remixing
 152 (Gray & Chugunov, 2006) where the coefficient c_D determines the strength of diffusion. The
 153 solid-fluid interaction term:

$$\beta^{G \leftrightarrow F} = (\mathbf{F}_i^b + \mathbf{F}_i^d) / V_M \quad (5)$$

154 is the sum of the buoyant force \mathbf{F}_i^b and the drag force \mathbf{F}_i^d , acting on size species i per unit
 155 volume. A more detailed evaluation of these forces is provided in Appendix A. We note that in
 156 the three-phase mixture model of Thornton et al. (2006), the fluid phase is only assumed to exert
 157 pressure on the surface of the particles. Here, we explicitly consider drag and buoyant forces
 158 which result from the relative motion of the solid and fluid phases. Since the interaction terms
 159 are internal forces, by Newton's Third Law, they should cancel as the mass and momentum
 160 equations are summed over all phases, i.e. $\beta^{L-S} + \beta^{S-L} = 0$ and $\beta^{G-F} + \beta^{F-G} = 0$.

161 Following Fan and Hill (2011b), the total stress experienced by a particle $\boldsymbol{\sigma}_i$ is further
 162 broken down into contact $\boldsymbol{\sigma}_i^c$ and kinetic $\boldsymbol{\sigma}_i^k$ components, representing the stresses which result
 163 from particle contacts and velocity fluctuations, respectively. As segregation occurs long after
 164 the bulk has reached a quasi-steady state, the temporal derivatives and inertial terms in the mass
 165 and momentum balance equations can be set to zero. Assuming that the flow is shallow and that
 166 segregation only occurs normal to the flow direction, the momentum equation can be reduced to:

$$0 = -\frac{\partial P_i^c}{\partial z} - \frac{\partial P_i^k}{\partial z} + \Phi_i \rho_i g \cos \theta - \Phi_i \rho_i c_{PI} (\mathbf{w}_i - \mathbf{w}) - \rho_G c_D \frac{\partial \phi_i}{\partial z} + \mathbf{F}_i^b / V_M + \mathbf{F}_i^d / V_M, \quad (6)$$

167 which can be simply denoted as:

$$0 = \Theta_i^{CS} + \Theta_i^{KS} + \Theta_i^W + \Theta_i^{PD} + \Theta_i^{FD} + \Theta_i^D. \quad (7)$$

168 Equation (7) implies that the forces acting on a particle phase i as it segregates are due to the
 169 partial contact stress gradient Θ_i^{CS} , partial kinetic stress gradient Θ_i^{KS} , particle-particle drag Θ_i^{PD} ,
 170 fluid drag Θ_i^{FD} , and diffusion Θ_i^D . Note that Θ_i^W is the buoyant weight that takes into account the
 171 fluid buoyant effect.

172 In recent segregation models, it is assumed that as the small particles percolate down into
 173 the granular matrix they bear less of the overburden pressure while the larger particles bear most
 174 of it as they are squeezed up. Therefore, to define the share of the pressure a solid phase in a unit
 175 granular mixture bears, the pressure fraction ψ_i is introduced. The contact and kinetic pressure
 176 borne by each phase per unit volume can thus be represented as fractions of the total contact and
 177 kinetic pressures:

$$\begin{aligned} P_i^c &= \psi_i^c P^c \\ P_i^k &= \psi_i^k P^k \end{aligned} \quad (8)$$

178 respectively. The pressure fractions ψ_i^c and ψ_i^k are assumed to satisfy the functional forms (Gray
 179 & Chugunov, 2006; Gray & Thornton, 2005):

$$\begin{aligned} \psi_{L,S}^c &= \phi_{L,S} \pm B^c \phi_S \phi_L, \\ \psi_{L,S}^k &= \phi_{L,S} \pm B^k \phi_S \phi_L, \end{aligned} \quad (9)$$

180 respectively, such that $\psi_L^{c,k} + \psi_S^{c,k} = 1$, and $\psi_i^{c,k} = 0$ for $\phi_i = 0$. The coefficients B_c and B_k are
 181 the magnitudes of the ‘overstress’, which lead the partial pressures to be away from the
 182 hydrostatic pressure and indicates the strength of the segregation driving force. These values are
 183 expected to be positive and are dependent on the size ratio, shear rate, and possibly many other
 184 variables (Weinhart et al., 2013; Staron & Phillips, 2015). The opposing signs represent the
 185 premise that different sized phases experience different and oppositely directed stresses. Note
 186 that recent work has pointed out the asymmetric dependence of ψ_i on ϕ_i (Gajjar & Gray, 2014;
 187 van der Vaart et al., 2015; Jing et al., 2017). Here the simplest linear form is adopted, as it is
 188 sufficient for mixtures of a moderate solid species concentration (Fan et al., 2014; Schlick et al.,
 189 2015).

190 2.2 Segregation velocity scaling

191 The segregation velocity $w_{p,i}$ is the rate at which large and small particles separate from
 192 each other. It may be derived from the momentum equations, substituting equation (8) into
 193 equation (6) while disregarding the solid-fluid interaction terms, which yields a segregation
 194 velocity model that is dependent of the kinetic stress gradients (Hill & Tan, 2011) and gravity
 195 (Gray & Thornton, 2005); a key assumption in this derivation is that the solid interaction term
 196 depends linearly on the relative velocity (equation (6)). Alternatively, in the literature the scaling
 197 of $w_{p,i}$ is often directly inferred, grounded in the underlying physics of segregation. Savage and
 198 Lun (1989) found that the segregation velocity of a species increases proportionally with the
 199 local concentration of the opposite species, $w_{p,i} \simeq 1 - \phi_i$, i.e. large particles rise up faster when
 200 it is in a region with a high volume concentration of small particles, showing the importance of
 201 local packing on segregation. Golick and Daniels (2009) found that $w_{p,i}$ decreases with
 202 increasing confining pressures highlighting the dependence of segregation on dilatancy and void
 203 generation. When $w_{p,i}$ is scaled with the local shear rate, a good collapse is achieved reflecting
 204 the dependence of segregation on the local deformation rate (Fan et al., 2014; Schlick et al.,
 205 2015, Jing et al., 2017). In search of a functional form to express the pressure-shear rate
 206 dependence of $w_{p,i}$, Fry et al. (2018) proposed a scaling of the following form:

$$w_{p,i}/\sqrt{g\bar{d}} = \pm AI(1 - \phi_i) \quad (10)$$

207 where \bar{d} is the mean particle diameter, A is a dimensionless constant, and $I = \dot{\gamma}\bar{d}\sqrt{\rho_G/P_G}$ is the
 208 inertial number commonly used to define the rheology of dense granular flows (Midi, 2004). The

209 basic form of this scaling relation has been shown to work for both size and density-driven
 210 segregation for a wide range of situations (Umbanhowar et al., 2019).

211 The sensitivity of $w_{p,i}$ on the rheology of granular flows leads one to suppose that a
 212 similar functional form can be acquired for segregation in ambient fluids when the rheology of
 213 solid-fluid mixtures can be taken into account or if fluid effects can be appropriately considered.
 214 We note that an expression for $w_{p,i}$ has already been proposed by Thornton et al. (2006) which
 215 suggests that fluid affects segregation only through buoyant effects in such a way that
 216 segregation weakens when ρ_F approaches ρ_G . Though qualitatively consistent with physical
 217 experiments (Vallance & Savage, 2000), it does not consider any other forms of solid-fluid
 218 interactions and the resultant flow rheology.

219 2.3 Dimensionless characterization of flow regimes for granular-fluid mixtures

220 The role of viscous fluids varies significantly in different flow regimes. Therefore, it is
 221 crucial in this work to explore a wide range of flow regimes that are relevant to natural saturated
 222 debris flows. In dry granular flows viscous forces are negligible and the time it takes for a
 223 particle to travel a distance d , under a confining pressure P can be estimated from the time it
 224 takes for it to freely fall in air, $t_{FF} = d/\sqrt{P/\rho_G}$. The dynamics of granular flows in this regime is
 225 controlled by the inertial number $I = d\dot{\gamma}/\sqrt{P/\rho_G}$ which is the ratio of the microscopic inertial
 226 time to the shear rate $\dot{\gamma}$. When the viscosity of the ambient fluid η_F is high, the motion of
 227 particles is significantly hindered by the viscous forces. The particle momentarily accelerates
 228 before finally reaching its viscous limiting velocity after a characteristic time $t_V = \rho_G/P$. The
 229 flow dynamics in this regime is now controlled by the viscous number $I_v = \eta_F\dot{\gamma}/P$. According to
 230 Courrech du Pont et al. (2003), granular-fluid flows can be classified according to three regimes

231 – free-fall (grain-inertial), fluid-inertial, and viscous. Each regime is characterized by unique
 232 solid-fluid interactions and are controlled by three dimensionless numbers – the Stokes
 233 number $St = I^2/I_v = \rho_G d^2 \dot{\gamma} / \eta_F$, the relative density $r_\rho = \sqrt{\rho_G / \rho_F}$, and the Reynolds
 234 number $Re = St / r_\rho$ – which express the relative importance of viscous and inertial forces on
 235 the flow rheology.

236 In the geophysical context, fluid-saturated granular flows can also be characterized
 237 according to the stresses and momentum transport processes which govern their motion. The
 238 Bagnold number $N_B = (\Phi \rho_G \bar{d}^2 \dot{\gamma}) / (1 - \Phi) \eta_F$ defines the relative dominance between
 239 collisional and viscous forces where \bar{d} is the mean particle diameter. The Savage number $N_S =$
 240 $(\rho_G \bar{d}^2 \dot{\gamma}^2) / (\rho_G - \rho_F) g H \tan \zeta$ is the ratio between collisional and frictional forces where ζ is the
 241 inter-particle contact friction angle and H is the granular flow height. The friction number $N_F =$
 242 $(\Phi (\rho_G - \rho_F) g H \tan \zeta) / (1 - \Phi) \dot{\gamma} \eta_F$ is the ratio between frictional and viscous forces. These
 243 dimensionless numbers are typically used to classify the dominant energy dissipation
 244 mechanisms in natural (Iverson, 1997) and experimental (de Haas et al., 2015; Zhou et al., 2019)
 245 debris flows and subaqueous sedimentary density flows (Mulder & Alexander, 2001). Iverson
 246 (1997) proposed limits to the magnitudes of these dimensionless numbers to define the transition
 247 from one dominant mechanism to another based on dry, cohesionless, granular-flow experiments
 248 (Bagnold, 1954; Savage & Hutter, 1989). Collisional forces dominate over viscous forces
 249 when $N_B > 200$; collisional forces dominate over frictional forces when $N_S > 0.1$; and when
 250 $N_F > 2000$ frictional forces dominate over viscous forces.

251 **3 Methods**

252 3.1 Model configuration and simulation parameters

253 Fully saturated, binary granular flows are simulated using the coupled discrete element
 254 method (DEM) and computational fluid dynamics (CFD). This method enables calculation of
 255 solid-fluid interactions at relatively low computational costs allowing for efficient three-
 256 dimensional simulations. Calculations involved in the CFD-DEM method are detailed in
 257 Appendix A. For the DEM part, binary granular flows are simulated as a mixture of two types of
 258 inelastic, frictional spheres of distinct particle sizes (small and large) flowing down a rough
 259 incline. Small and large particles are set to have average diameters of $d_S = 0.005m$ and $d_L =$
 260 $0.01m$ respectively. A slight poly-dispersity is introduced to each particle size to prevent
 261 geometrical ordering. This is implemented by randomly generating particles with diameters that
 262 are uniformly distributed around their mean value in such a way that $\frac{(d_{L,S}^{max} - d_{L,S}^{min})}{d_{S,L}} = 0.1$ where
 263 d^{max} and d^{min} are the maximum and minimum diameters allowable for each particle size. The
 264 floor is roughened by ‘gluing’ a random array of small particles and no bounding walls are set at
 265 the top surface. This roughness condition ensures minimal slippage at the base. All DEM
 266 simulation domains are set to have a length, width, and height of $35d_S \times 10d_S \times 40d_S$. The size
 267 ratio and large particle concentration are held constant with values of 2 and 0.5, respectively,
 268 throughout all simulations since our focus is the fluid effects. Particles are initially normally
 269 graded – large particles locate at the base and small particles locate at the top.

270 Figure 1a shows the schematic diagram of the system being simulated and the
 271 corresponding coordinate system. Periodic boundary conditions are set along the flow direction
 272 representing an infinitely long chute and granular flows are initiated from rest by tilting the xy

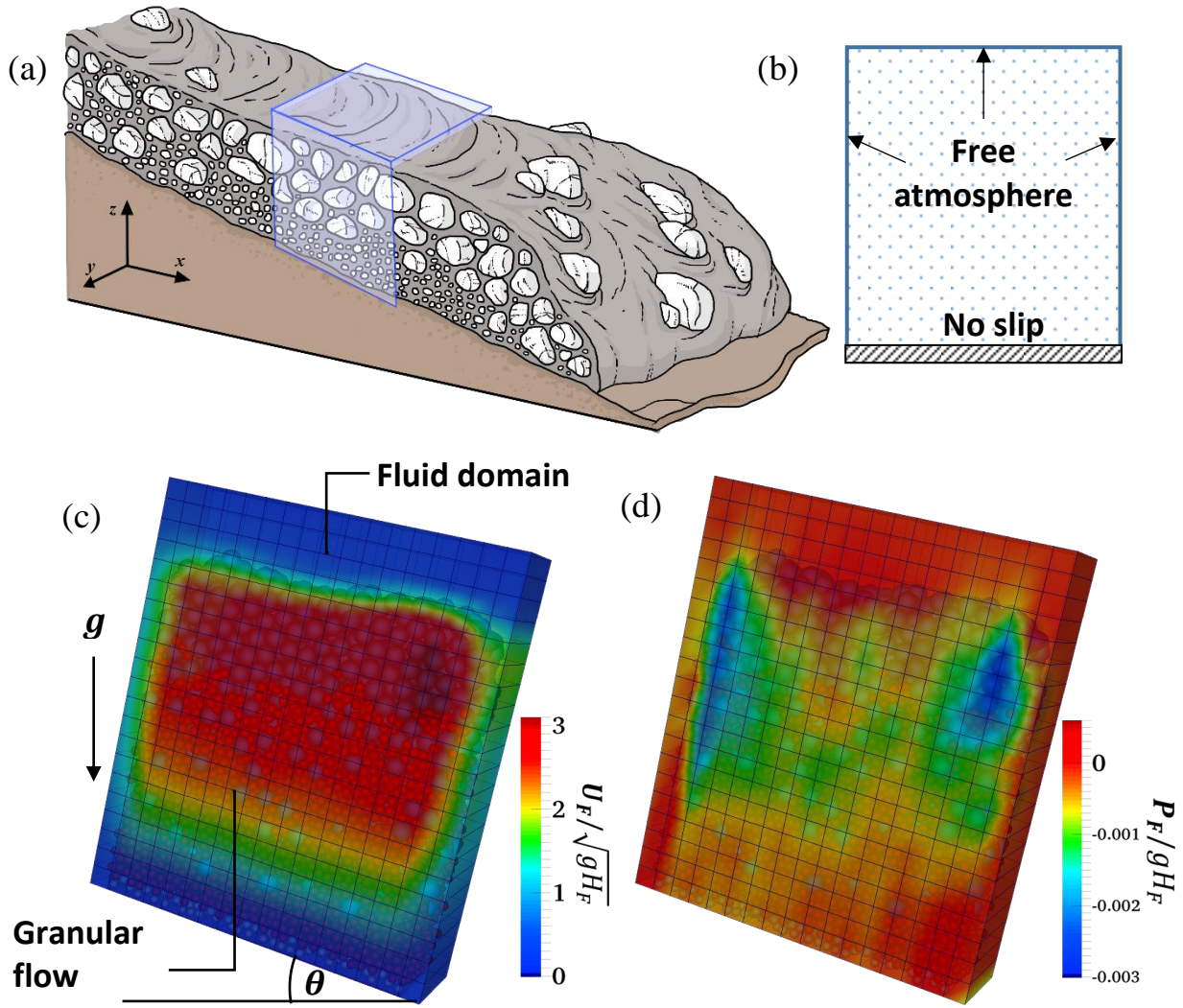


Figure 1. (a) A schematic diagram showing the simulated system – a fully saturated debris flow – and the coordinate system for a fixed section, indicated by the box. (b) Boundary conditions of the boxed domain in (a). Snapshots of (c) normalized fluid velocity $U_F/\sqrt{gH_F}$ and (d) pressure P_F/gH_F .

273 plane to a designated angle of inclination. The DEM solver in use can only set periodic
 274 boundaries in one direction at a time and hence rigid walls have to be placed lateral to the flow
 275 direction. Interactions between the lateral walls and the particles are set to be completely elastic
 276 and frictionless with the particle-wall contact stiffness equal to those between inter-particle
 277 collisions. We have verified that no velocity nor pressure gradients formed near the sidewalls.

278 Although wall-effects cannot be totally ruled out, they are found to have little effect on the
279 segregation process and do not significantly change the main conclusions drawn from this work.

280 The fluid domain is an incompressible Newtonian fluid, uniformly discretized in such a
281 way that at least five large particles would fit (Zhao et al., 2014). The fluid is ambient – it only
282 responds to the drag exerted by the particles and does not flow on its own under gravity. As
283 illustrated in Figure 1b, the state of ambience is obtained by adopting the free-atmosphere
284 boundary condition at the right, left and top walls. Pressure is computed based on the local
285 velocity of adjacent meshes where it is given a value p_0 if the flow is going out of the domain
286 and $p_0 - 0.5|\mathbf{U}_F^2|$ for inflow; velocity dynamically changes from zero gradient when there is an
287 outflow to flux dependent, computed as $-\nabla P_F$, when there is an inflow. This allows the fluid to
288 freely flow in and out of the domain. A non-slip condition (zero pressure gradient, fixed zero
289 velocity) is set at the bottom wall.

290 The complete simulation set-up is shown in Figure 1c where the solid domain is
291 positioned completely within the fluid domain. The fluid is initially static and only flows as it is
292 dragged by the particle motion. The normalized fluid velocity $\mathbf{U}_F/\sqrt{gH_F}$ fields (where H_F is the
293 fluid height) match with the regions occupied by the moving grains, and therefore does not exert
294 an external shear at the top surface of the granular flow. The rheology is completely controlled
295 by the internal deformation of particles. Figure 1d, shows the distribution of the normalized
296 dynamic component of the pore pressures \mathbf{P}_F/gH_F within the granular flow. These pressures
297 fluctuate rapidly with time wherein negative values correspond to shear expansion and positive
298 values denote shear contraction. The negative pressure spikes at the edges of the granular flow

Table 1. *Model Input Parameters*

DEM Parameter	Value	Simulation parameter	Value
Young's modulus E (Pa)	5×10^{-7}	Simulation time t (s)	$10^2 - 10^3$
Poisson's ratio	0.35	DEM time step size Δt (s)	1×10^{-5}
Density ρ_s (kg/m ³)	2650	Coupling frequency *	10
Particle friction angle (°)	30		
Damping coefficient β	0.05		

*Coupling frequency is the number of the DEM iterations in one coupling interval.

299 domain (since the fluid domain is set slightly longer than the solid domain) result from the
300 relative motion of the solid grains and the fluid (Zhao, 2017).

301 DEM particle and simulation parameters are kept constant throughout all simulations and
302 are summarized in Table 1. It should be noted that, in order to minimize computation time,
303 Young's modulus used in this study is lower than those of real glass beads. However, according
304 to previous computational studies (Hill & Tan, 2014; Staron & Phillips, 2015; Jing et al., 2019)
305 and some preliminary tests conducted, the choice of E , over a range of 10^7 - 10^9 Pa, does not
306 significantly affect the flow properties at steady-state nor does it influence the development of
307 size segregation. No cohesive forces resulting from the presence of ambient fluid is considered in
308 the simulations.

309 3.2 Test set-up

310 The different flow regimes enumerated in II.C are simulated by varying the fluid density
311 and viscosity. Mixtures flowing at different angles of inclination are simulated for each regime.

Table 2. *Test Setup*

Flow regimes	Inclination θ	$[\rho_F \text{ (kg/m}^3\text{)}, \eta_F \text{ (kg/m}\cdot\text{s)}]$
Free-fall (FF)		$[1.29, 1.85 \times 10^{-5}]$
Fluid-inertial (FI)	$[22, 24, 26, 28, 30, 32]^\circ$	$[1000, 1 \times 10^{-3}]$
Viscous (VI)		$[1000, 0.5]$

312 The free-fall (FF) regime corresponds to the dry case where the interstitial fluid is air and will
313 serve as points of comparison as size segregation in dry granular chute flows have already been
314 extensively studied (e.g. Tripathi & Khakhar, 2011; Tunuguntla et al., 2016; Jing et al., 2017). In
315 the fluid-inertial (FI) regime, the ambient fluid is water at 20°C where the viscous forces are not
316 high enough to dominate inertial effects for the latter to be completely ignored. A fluid 500 times
317 more viscous than water is used in the viscous (VI) regime. This fluid is still Newtonian and has
318 the same density as water. Such a fluid can be likened to the fine particle-rich slurries found in
319 natural debris flows (Major & Pierson, 1992; Zhou & Sun, 2017) after it has already yielded. The
320 fluid inertial and viscous regimes will be collectively referred to as the saturated regimes. The
321 entire test setup is summarized in Table 2.

322 Segregation in different flow regimes will be analyzed according to the forcing terms
323 enumerated in equation (7) and segregation velocities. As such, properties like the partial stress
324 gradients, pressure fractions, flow velocities, shear rates, drag forces, etc. need to be calculated
325 from DEM and CFD data. The method for calculating the said properties are detailed in
326 Appendix B. It should be mentioned that the calculation of the contact pressure P^c is dependent
327 on the manner at which forces are partitioned between differently sized particles. In this study,
328 forces are partitioned according to the volume ratio of the contacting particles (Tunuguntla et al.,

2014) whereas several previous works partition the forces at the point of contact (i.e., according to the radius ratio of contacting particles) (Fan & Hill, 2011b; Staron & Phillips, 2015; Weinhart & Thornton, 2017). More information on the calculation and effects of the different contact force partitioning methods are presented in Appendix C. Likewise, the method for estimating the linear drag c_{PI} and diffusion coefficients c_D , which are necessary for the calculation of particle interaction forces, is discussed in detail in Appendix D.

4 Results

4.1 Dimensionless characterization of flow regimes

Simulated saturated granular flows are plotted in the (St, r_p) space as shown in Figure 2a. Each point falls within a specific flow regime bounded by limits proposed by Courrech du Pont et al. (2003) (solid lines) and Cassar et al. (2005) (dotted lines) which mark the transition from one regime to another. These points are calculated during rapid segregation time which will be defined in IV.B. To cast them into the light of actual geophysical flows, the Re values of the simulated flows are plotted against their N_B , N_S and N_F values as shown in Figures 2b, c, and d respectively. The dotted lines represent the boundaries proposed by Iverson (1997) and the gray areas are the range of values for the given dimensionless numbers obtained for natural debris flows (de Haas et al., 2015).

Flows in the FF regime are highly collisional and are primarily driven by grain-inertial forces as indicated by their very high Re and N_B values (Figure 2b). This is not surprising as the fluid in such cases are negligible such that they virtually do not affect particle motion. Flowing at relatively low angles of inclination, these flows are dense, more frictional than collisional as suggested by their N_S (Figure 2c). Increasing the flow velocity (by increasing the angle of

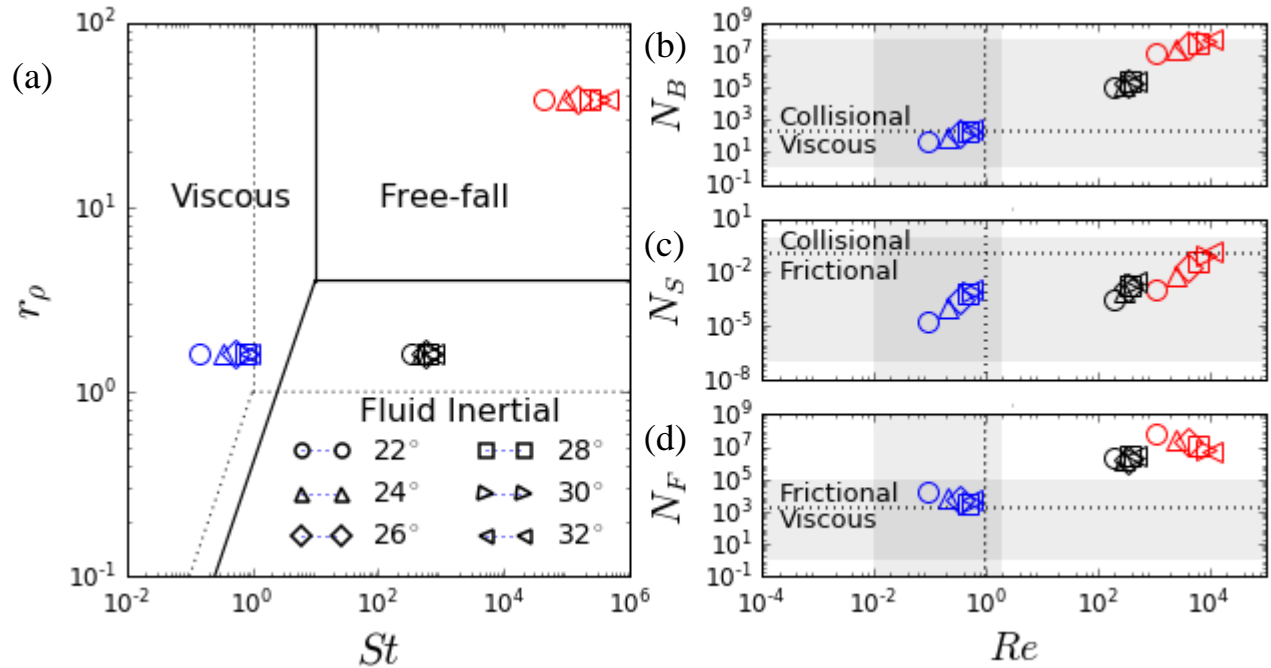


Figure 2. (a) Flow regimes of solid-fluid mixture flows projected in the (St, r_ρ) space. Solid lines represent the limits proposed by Courrech du Pont et al. (2003) which represent $St = 10$, $r_\rho = 4$ and $Re = 2.5$. Dotted lines are those assumed by Cassar et al. (2005) where $St = r_\rho = Re = 1$. (b-d) Simulated cases characterized by the dimensionless numbers for geophysical flows: (b) Bagnold number N_B , (c) Savage number N_S , and (d) Friction number N_F . Dashed lines represent the limits proposed by Iverson (1997) and shaded regions represent the ranges of the dimensionless numbers of natural debris flows summarized in de Haas et al. (2015). Symbols used in all plots represent the simulated cases at different angles of inclination ($\theta = [22, 24, 26, 28, 30, 32]^\circ$).

351 inclination) makes the flows increasingly collision dominated. This is further supported by
 352 their N_F values where they become even more frictional than typical experimental and natural
 353 debris flows (Figure 2d).

354 The values of Re of the simulated FI flows are above the limits obtained for natural
 355 debris flows but are comparable to those of small-scale debris flow experiments (Iverson, 1997;
 356 de Haas et al., 2015). Their N_B values suggest that these flows are still highly collisional despite
 357 the presence of water (Figure 2b) but are more frictional than collisional based on the N_S values

358 (Figure 2c). This means that the viscous damping exerted by water is not enough to significantly
 359 inhibit grain-inertial effects but is enough to make them more frictional than subaerial flows
 360 (free-fall regime flows). The N_B and N_S values of the simulated fluid-inertial flows are
 361 comparable to those of typical natural debris flows (Figures 2b and c) approaching the limit of
 362 granular, hyperconcentrated density flows (Mulder & Alexander, 2001)

363 The dimensionless numbers of the simulated VI flows are close to natural debris flows
 364 but are lower than experimental debris flows. Their N_B values are consistently below the limit of
 365 viscous flows and their Re values suggest that grain-inertial effects are significantly low and
 366 these flows can be considered as ideally viscous (de Haas et al., 2015) (Figure 2b). Viscous
 367 damping becomes more significant in such flows making it increasingly frictional (Figure 2c).
 368 Measured friction numbers N_F however suggest that frictional forces still dominate over viscous
 369 forces (Figure 2d). This is due to the fact that shearing among particles is still due to the flow's
 370 downward motion by gravity and is only slightly viscous since the fluid itself is simply reactive
 371 to the granular flow.

372 4.2 Process of segregation

373 The degree of segregation, indicating how well the two particle-size species separate, is
 374 defined as the relative distance of separation between the large and small particles' centers of
 375 mass (Jing et al., 2017):

$$\alpha(t) = 0.5 \left(1 - \frac{C_{L,t} - C_{S,t}}{C_{L,0} - C_{S,0}} \right) \quad (11)$$

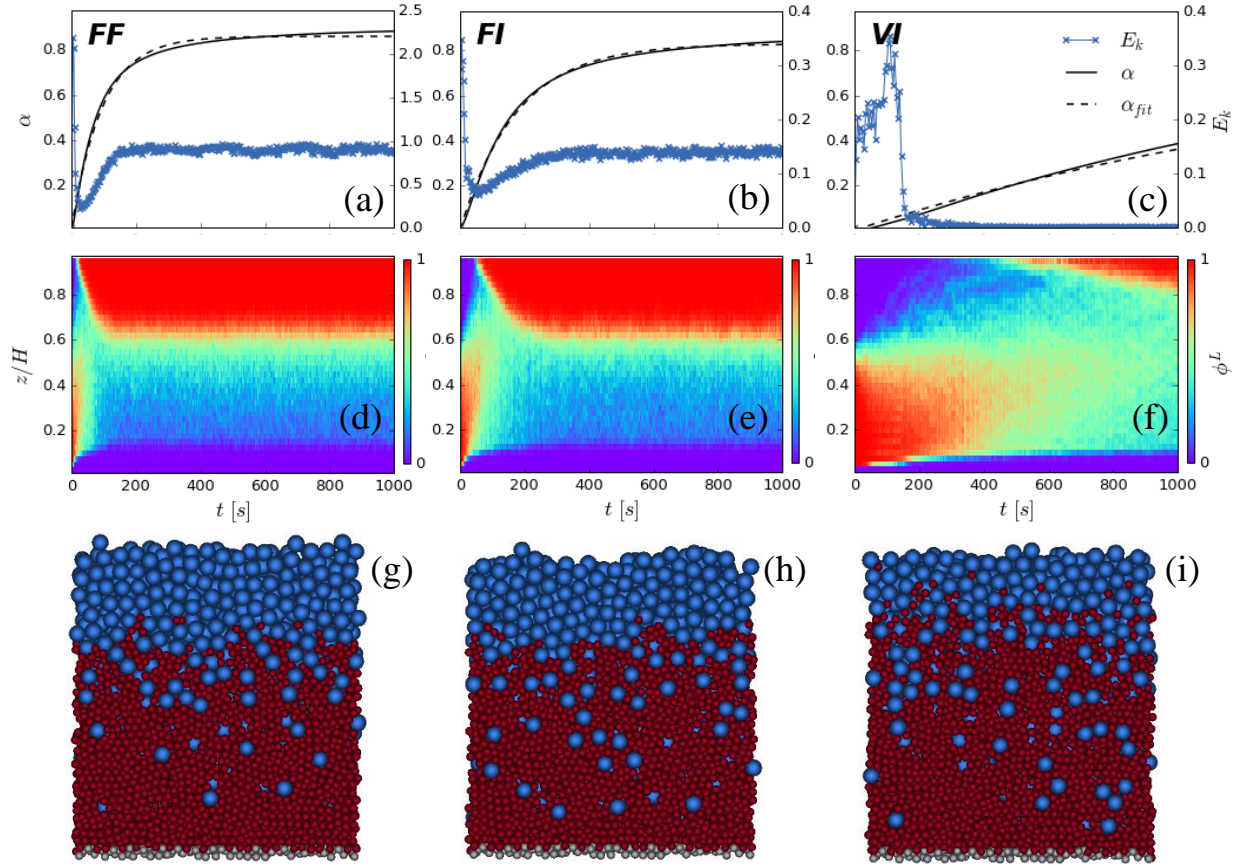


Figure 3. Arranged from top to bottom are (a-c) time evolution of the degree of segregation α and flow kinetic energy, (d-f) spatial-temporal distribution of the large particle concentration ϕ^L , and (g-i) final deposit profiles of the bi-disperse mixtures flowing at $\theta = 22^\circ$ for different flow regimes. Dashed lines in (a-c) represent the fit obtained from equation (12).

376 where $C_{L,t}$ and $C_{S,t}$ are the bulk centers of mass of the large and small particles at time t ,
 377 respectively, while $C_{L,0}$ and $C_{S,0}$ are the initial bulk centers of mass. A value of 1 represents
 378 perfect segregation, which means that the centers of mass of the two phases have completely
 379 reversed, while a value of 0 indicates that the mixture has not progressed from its initial state.
 380 Figures 3a-c show the evolution of α and granular flow kinetic energies E_k for the FF, FI, and VI
 381 regimes, respectively. At early times, α rapidly increases and slows down at a later point up until
 382 it reaches a steady state. The time evolution of α follows an exponential trend which can be fit
 383 to:

$$\alpha(t) = \alpha_f(1 - e^{-t/\tau_s}) \quad (12)$$

384 where α_f is the final degree at steady state, and τ_s is the dimensionless characteristic timescale
 385 associated with the segregation rate (Hill & Tan, 2014; Staron & Phillips, 2015) and reflects how
 386 fast segregation develops. Segregation is said to develop faster when the values of τ_s is small,
 387 and slower otherwise. To illustrate how well α represents the process of segregation, the
 388 corresponding spatial-temporal profiles of the large particle concentration ϕ_L are plotted in
 389 Figures 3d-f for the FF, FI, and VI regimes, respectively. Snapshots of the three segregated
 390 mixtures at the end of the simulation are shown in Figures 3g-i. Due to computational limitations
 391 all simulations have only been run up to $t = 1000s$, by which time segregation in VI is still
 392 incomplete. Nevertheless, in this study we are more interested in the segregation process rather
 393 than the steady state and we focus on the time when segregation is still underway.

394 Figure 4a shows that the α curves for a similar angle (22°) belonging to different flow
 395 regimes can be cast into a single time frame when they are plotted against the dimensionless
 396 time t/τ_s . The shaded area represents a period of time $t = 0 \sim 0.5\tau_s$ in which segregation in the
 397 three regimes can be considered to develop at the same pace. The value of α achieved at $0.5\tau_s$
 398 (denoted as $\alpha_{0.5\tau_s}$) for all θ are plotted in Figure 4b, showing that the degree of segregation
 399 generally decreases with the inclination but are comparable across different flow regimes. For
 400 the FF and FI cases, maximum segregation is achieved at the lowest angle $\theta = 22^\circ$, while for the
 401 VI cases, optimal segregation occurs at a medium angle $\theta = 24^\circ$, after which α declines steadily.

402 Figure 4c shows the segregation time scale τ_s (inversely, the characteristic segregation
 403 rate) for the three flow regimes. Interesting trends are observed. In dry cases (FF regime), τ_s

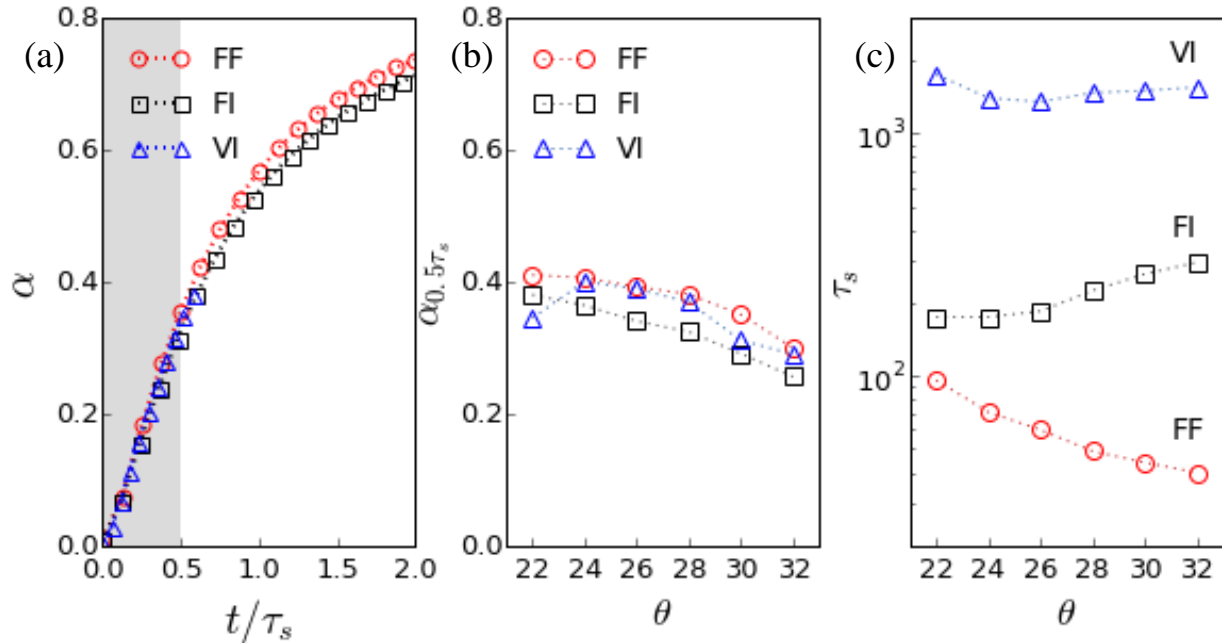


Figure 4. (a) Evolution of the degree of segregation α for $\theta = 22^\circ$ for all flow regimes in dimensionless time t/τ_s . The gray region indicates the span of time in which the segregation in the three regimes develop simultaneously. (b) $\alpha_{0.5\tau_s}$ vs. θ and (c) τ_s vs. θ for all flow regimes.

404 decreases as θ is increased; qualitatively, this can be understood as faster flows result in faster
 405 void generation and kinetic sieving (Drahn & Bridgwater, 1983). In saturated cases, τ_s is
 406 generally increased, consistent with previous chute flow experiments of Vallance and Savage
 407 (2000). However, the trend of τ_s with θ is reversed in the saturated regimes where segregation
 408 instead develops over longer periods of time when θ is increased. To investigate this, we look
 409 into the flow rheology and driving forces in the momentum equations which are measured during
 410 the segregation process.

411 4.3 Mixture flow rheology

412 Figure 5 shows the profiles of the bulk flow velocity u , shear rate $\dot{\gamma}$, contact pressure P^c ,
 413 and kinetic pressure P^k of all cases. These profiles are averaged over $t = 0.1 \sim 0.5\tau_s$ where
 414 segregation is considered to develop rapidly and the initiation effects are minimal. The pressures

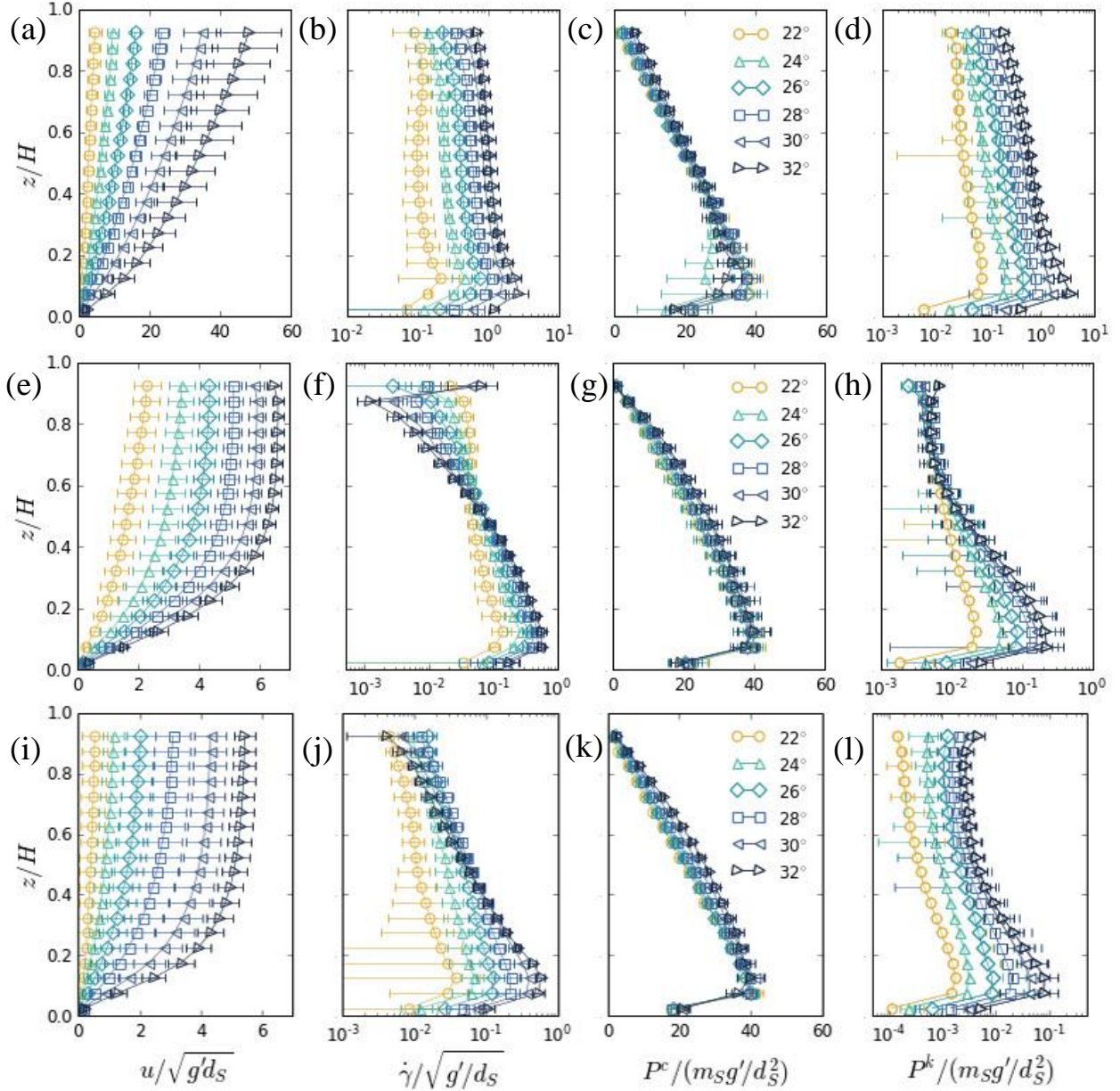


Figure 5. Dimensionless, time-averaged u , $\dot{\gamma}$, P^c , and P^k profiles of granular-fluid flows in the (top) FF, (middle) FI, and (bottom) VI flow regimes for different angles of inclination. Averaging is done over the time when segregation is rapid.

415 are normalized by $m_S g'/d_S^2$ where m_S and d_S are the small particle mass and diameter,
 416 respectively, and $g' = (\rho_G - \rho_F)g/\rho_G$ is the reduced gravity due to buoyancy. u and $\dot{\gamma}$ are
 417 normalized by $\sqrt{g'd_S}$ and $\sqrt{g'/d_S}$, respectively. The z coordinate is normalized by the granular
 418 flow height H . The error bars represent the standard deviations of the measured quantities.

419 In the FF regime, u increases with θ and shows no slippage near the base (Figure 5a), $\dot{\gamma}$
420 varies linearly along the height except near the base and also increases with θ (Figure 5b), P^c
421 increases towards the base and only changes slightly with θ (Figure. 5c), and P^k , which
422 measures random particle fluctuations, scales similarly with the shear rate (Figure 5d). The
423 shapes of all rheological profiles do not significantly vary for different values of θ but
424 consistently increase in magnitude.

425 In the FI regime, plug zones are observed near the free surface of the u profiles (Figure
426 5e). This flow feature is similar to what is observed in subaqueous laboratory sediment flows
427 (Ilstad et al., 2004) and experimental debris flows (Mainali & Rajaratnam, 1994). We attribute
428 the origin of plug zones to the fluid drag force in the flow direction, which changes the
429 rheological behavior of the flows (more data are provided in Appendix C). The plug zone
430 corresponds to an area of very low $\dot{\gamma}$ in which the velocity differences between flowing layers
431 are small (Figure 5f). P^k in this regime is lower by about an order of magnitude compared to
432 that in FF, implying that the random fluctuating motion of both particle species are greatly
433 suppressed (Figure 5h). Below the plug zone, u rapidly decreases as it approaches the base,
434 corresponding to the rapid increase of $\dot{\gamma}$ and P^k . P^c , being normalized by g' , has the same
435 magnitude as that of the FF regime, showing that the ambient fluid reduces the magnitude of the
436 normal contact forces between particles (Figure 5g), i.e., a hydrostatic buoyant effect. The
437 dynamic component of buoyancy along the normal direction is found to be negligible.

438 In the VI regime, u values are only slightly lower than those in FI and similar plug zones
439 are observed (Figure 5i). $\dot{\gamma}$ is observed to increase with θ up to 28° and start to decrease at higher
440 angles between 30° and 32° (Figure 5j). These rheological behaviors are linked to the fluid-

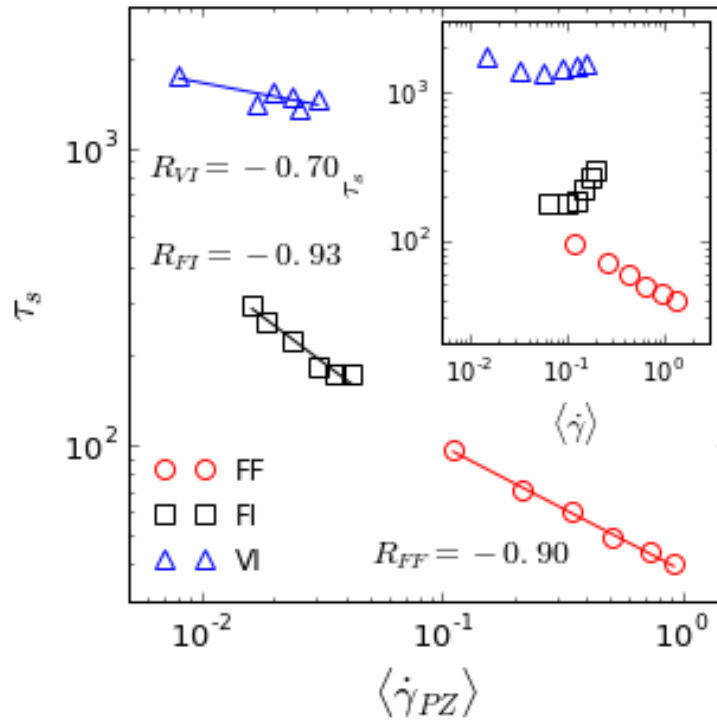


Figure 6. The relationship between the segregation timescale τ_s and the averaged shear rate measured in the plug zone $\langle \dot{\gamma}_{PZ} \rangle$ and (inset) along the entire flow depth $\langle \dot{\gamma} \rangle$. The strength of correlation between these two values is measured by the Pearson coefficient R . Fitting lines are obtained using the equation $y = ax^b$.

441 particle interactions in the VI regimes and are explained in more detail in Appendix C. P^k is
 442 lower by an order of magnitude relative to FI (Figure 5l). P^c is still of the same magnitude as
 443 with the previous two regimes and vary only slightly with θ , since the buoyant effect is a
 444 function of the relative density of the solid and fluid phases and is independent of the fluid
 445 viscosity (Figure 5k).

446 To link segregation with the flow rheology, $\dot{\gamma}$ is plotted against the segregation
 447 timescale τ_s as shown in Figure 6. The $\dot{\gamma}$ is singled out among all rheological profiles since it is
 448 the one showing the greatest sensitivity to the flow conditions and, as reported in several
 449 previous studies (May et al., 2010; Staron & Phillips, 2014), is strongly related to the segregation
 450 timescale. The inset of Figure 6 shows that the depth-averaged shear rate $\langle \dot{\gamma} \rangle$ generally increases

451 with θ in all flow regimes and thus, as with Figure 4c, τ_s decreases in FF but increases in FI and
 452 VI as $\langle \dot{\gamma} \rangle$ increases. Plotting τ_s against $\langle \dot{\gamma}_{PZ} \rangle$, which is the average shear rate in the plug zone
 453 (which occupies approximately the upper half of the $\dot{\gamma}$ profile excluding the topmost points),
 454 yields consistently decreasing trends across all flow regimes with strong negative correlations
 455 (shown as Pearson R correlation coefficients in Figure 6). The changes of $\langle \dot{\gamma}_{PZ} \rangle$ with θ in VI is
 456 consistent with the non-monotonic trend of τ_s – the decrease of $\langle \dot{\gamma}_{PZ} \rangle$ starting from $\theta = 28^\circ$
 457 matches the increase of τ_s at the same angle. This implies that in addition to the reduction of
 458 total $\dot{\gamma}$ across different flow regimes, segregation is also sensitive to the formation of fluid-
 459 induced rheological features such as plug zones.

460 4.4 Momentum balance source terms

461 Figure 7 shows the depth-averaged ‘forces’ acting on the rising large particles in the
 462 normal direction for mixtures flowing at 22° for $t = 0 \sim 0.5\tau_s$ (the shaded region in Figure 4a).
 463 These forces correspond to the source terms on the right-hand side of equation (7). In this way,
 464 the forces acting on the large particles can be compared directly during the time in which
 465 segregation in the three flow regimes occur at the same pace, facilitating the isolation of different
 466 fluid effects and comparison of their magnitudes with those induced by particle interactions. All
 467 force terms are normalized by the buoyant weight prior to depth averaging to take into account
 468 the buoyant effect.

469 At the onset of segregation the partial contact stress gradient Θ^{CS} is larger than the bulk
 470 buoyant weight Θ^W (see, e.g., Figure 7a), and therefore drives the large particles upward. By
 471 contrast, the kinetic stress gradient Θ^{KS} remains small in all stages. As segregation proceeds, Θ^{CS}
 472 decreases as more particles rise up to the free surface. It is interesting to note that the difference

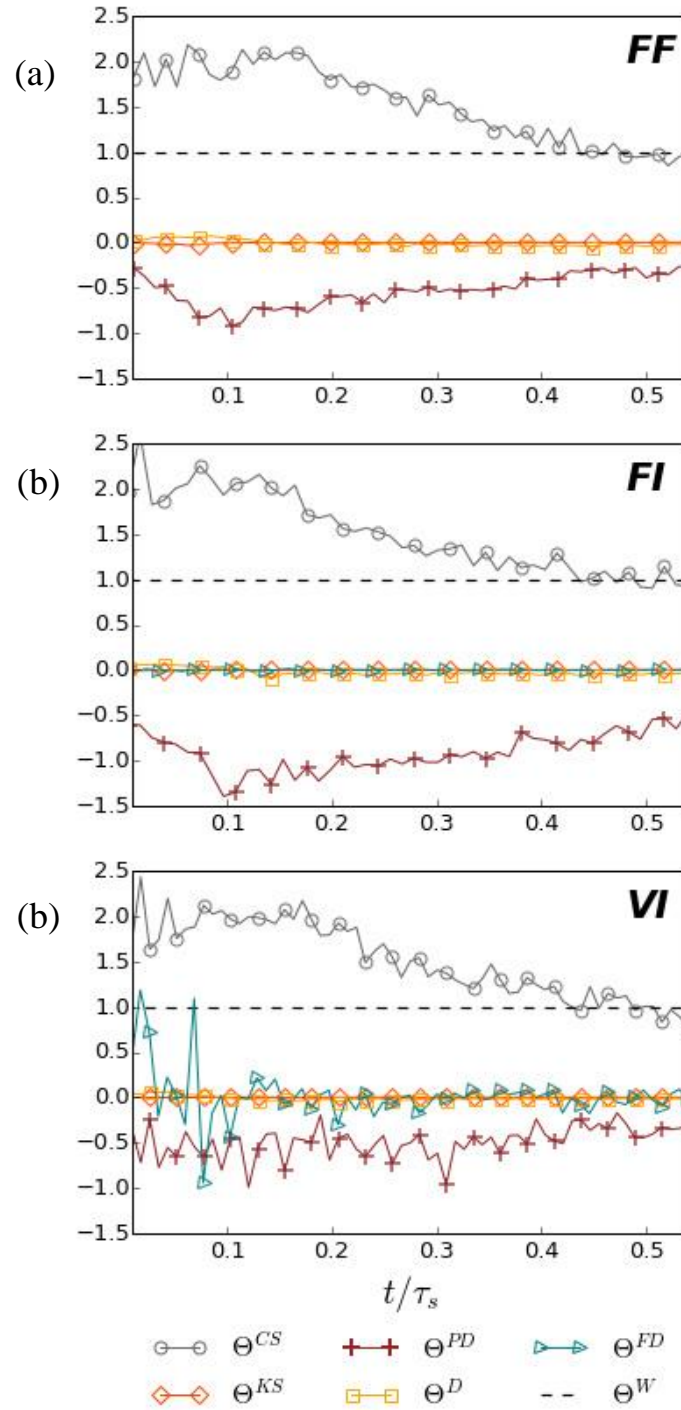


Figure 7. Time evolution of the force terms experienced by large particles according to equation (7).

473 between θ^{CS} and θ^W are comparable in all three flow regimes (Figures 7a-c), indicating that

474 buoyancy reduces the weight and the partial pressure gradient in a similar way. Therefore, it can

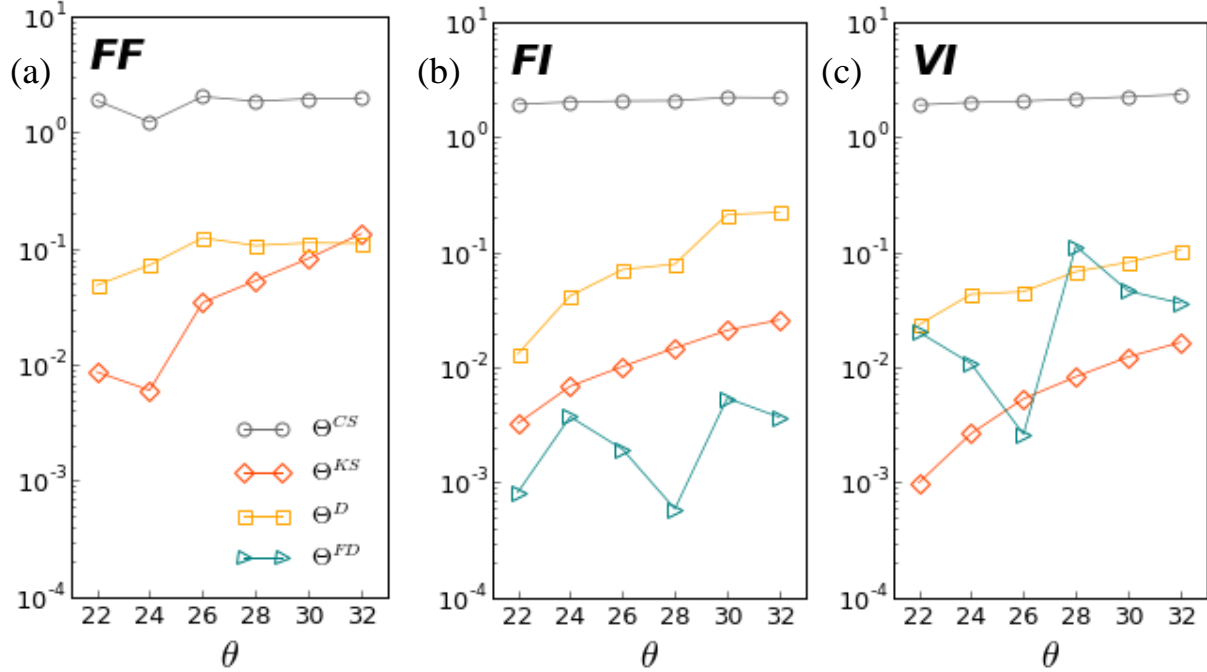


Figure 8. Magnitude of the mean forces acting on the large particles in the (a) FF, (b) FI, and (c) VI regimes as functions of θ .

475 be concluded that the buoyant effect mainly acts as a scale factor for gravity, which warrants the
 476 use of the reduced gravity g' .

477 The difference between Θ^{CS} and Θ^W is mainly balanced by the particle-particle drag, Θ^{PD}
 478 (and only slightly by the diffusive force Θ^D), while the fluid-particle drag Θ^{FD} is practically
 479 negligible in both two saturated regimes (with larger fluctuations in the VI regime). The latter is
 480 a surprising result as the fluid viscosity in the VI regime is high. Close evaluation of the fluid
 481 drag force shows that, since segregation proceeds slowly in the VI case, the drag forces are
 482 negligible owing to the very small relative velocities between the large particles and the fluid
 483 along the normal direction.

484 To understand the dependence of the segregation time on the slope angle (Figure 4c), we
 485 average each force term over $t = 0 \sim 0.2\tau_s$ for all simulated cases and plot their absolute values
 486 against θ in Figure 8. The choice of this time span is quite arbitrary and is only considered since

487 it corresponds to the time in which Θ^{CS} is the highest in all simulated cases. Figure 8 shows that
 488 Θ^{CS} is similar in magnitude and varies only slightly with θ regardless of the flow regime,
 489 while Θ^{KS} , although small in magnitude, increases significantly with θ . The level of diffusion
 490 (Θ^D) steadily increases with θ even with the presence of a viscous fluid and is roughly of the
 491 same order of magnitude relative to Θ^{KS} in each flow regime. In the saturated regimes, Θ^{FD}
 492 values are consistently low and show no clear dependence on θ .

493 Results in Figures 7 and 8 suggest that segregation occurs when the partial normal stress
 494 gradient in the mixture overcomes the pull of gravity, as is the premise of gravity-driven
 495 segregation theory (Gray & Thornton, 2005). This is a robust result across the three distinct flow
 496 regimes, as long as the buoyant effect is taken into account. However, within each flow regime,
 497 the dependence of the segregation time scale on the inclination angle (hence local shear rates)
 498 cannot be explained by this argument because Θ^{CS} only varies mildly with θ , which does not
 499 match the trend of τ_s with θ . Furthermore, Θ^{CS} decays toward and even below Θ^W far before the
 500 process of segregation completes (Figure 7). This indicates that the depth-averaged stress
 501 gradient, although capturing the fluid buoyant effect, may smear out fine details regarding
 502 distributions of the local concentration and the local shear rate, a point we address further below.

503 4.5 The overstress coefficient B

504 As the dependence of segregation driving force on θ is not well-captured by depth-
 505 averaging, a more localized approach is adopted here to take into account the local concentration.
 506 According to the gravity-driven segregation theory, segregation occurs only when the fraction of
 507 the pressure ψ_i experienced by a particle species is greater than what the local concentration ϕ_i
 508 can support. This relationship is expressed using equation (9) where the partition coefficient B

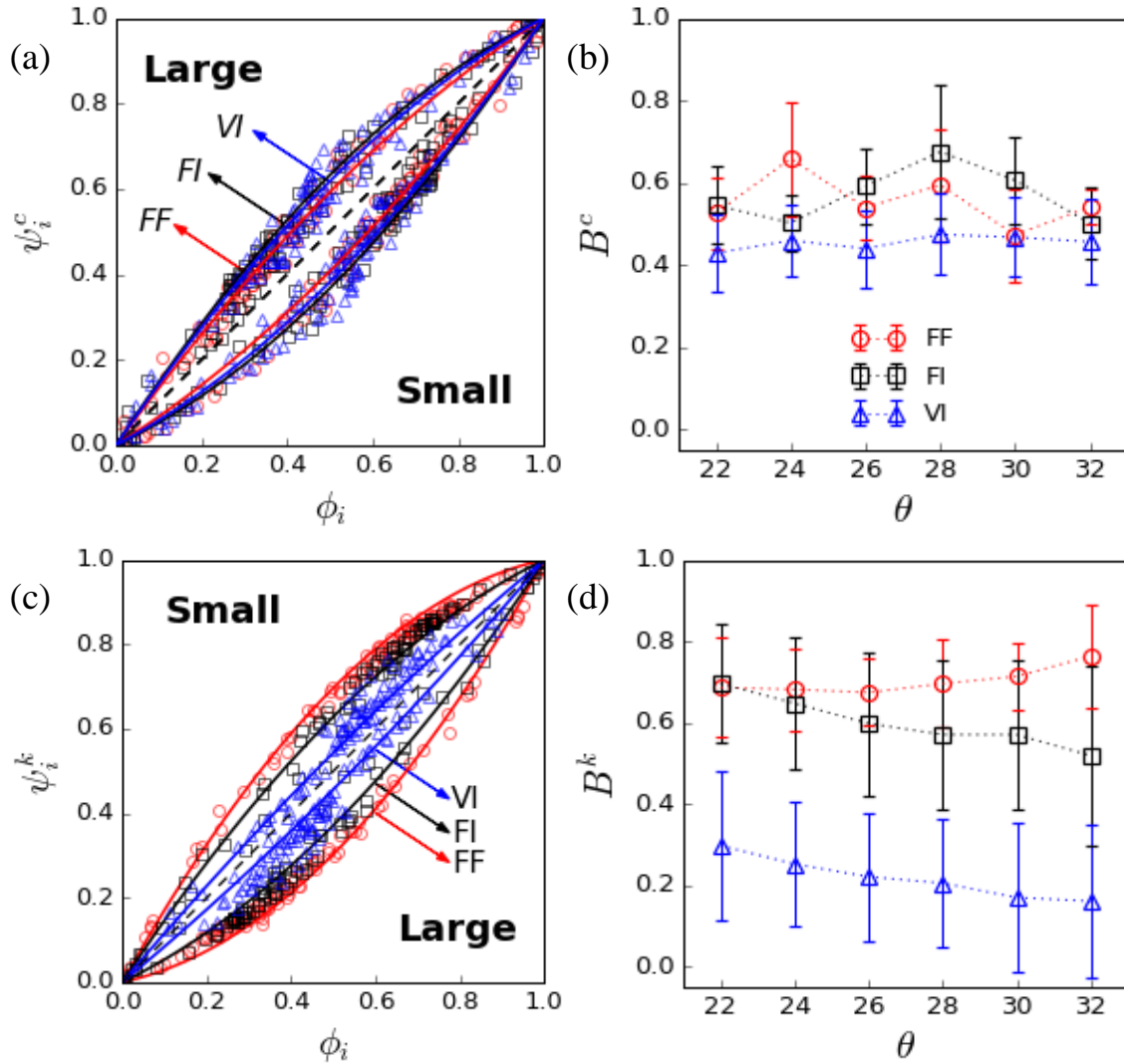


Figure 9. (a) Contact stress fraction ψ_i^c as a function of the volume concentration ϕ_i during rapid segregation of mixtures flowing at 22° in different flow regimes. (b) B^c values as a function of θ . (c) Kinetic stress fraction ψ_i^k vs ϕ_i and (d) B^k as a function of θ .

509 indicates by how much ψ_i is greater than ϕ_i and hence measures how strong the segregation
 510 driving force is. This analysis is applied for both contact and kinetic pressures.

511 The contact stress fraction ψ_i^c for different flow regimes ($\theta = 22^\circ$) are plotted as
 512 functions of ϕ_i in Figure 9a. The contact stress fraction of large particles are larger than their
 513 concentrations, which means that the large particles bear more of the contact pressure relative to
 514 the small particles. The $\psi_i^c - \phi_i$ curves of the FF, FI, and VI regimes are closely overlapping,

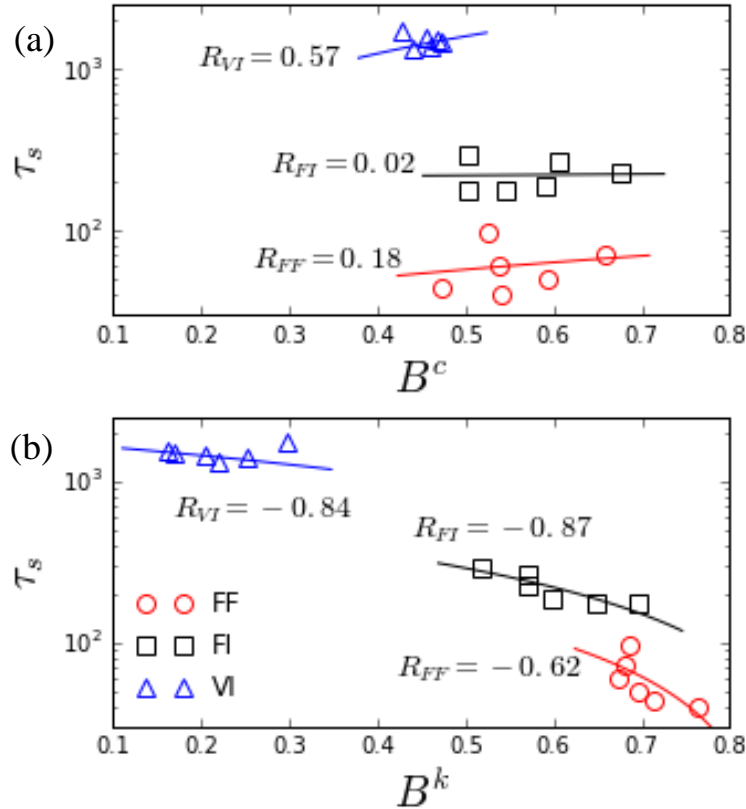


Figure 10. The relationship between τ_s and (a) contact B^c and (b) kinetic B^k overstress coefficients, with the strength of correlation measured by the Pearson coefficient R . Fitting lines are obtained using the equation $y = ax^b$.

515 where positive B^c values of 0.58, 0.56 and 0.47 for the large particles are obtained, respectively,
 516 suggesting that the biased contact stress distribution act in the same direction of their upward
 517 motion. (Note that these values are significantly higher than those reported in Hill and Tan
 518 (2014), due to the different partitioning criteria applied; see Appendix B2.) Figure 9b shows
 519 that B^c is essentially independent of θ , and is noticeably lower in the VI regime than in the FF
 520 and FI regimes. Figure 10a shows that B^c is only weakly correlated with τ_s , which is similar to
 521 the correlation regarding Θ^{CS} in Figure 8.

522 The relationship between the kinetic stress fraction ψ_i^k and ϕ_i is shown in Figure 9c.
 523 Fitting equation (9) for the large particles yields negative values of $B^k = -0.72, -0.70$ and
 524 -0.35 for the FF, FI, and VI regimes respectively. Positive B^k values for the small particles

525 mean that they are the ones bearing more of the kinetic pressure. Figure 9d shows that B^k
 526 increases with θ in the FF regime but decreases in the fluid-saturated regimes. B^k also decreases
 527 as the flow becomes more viscous – it is highest in the dry FF regime and lowest in the VI
 528 regime. This is consistent with the global decrease in P^k by orders of magnitude, observed in
 529 Figure 5, as the flows become more viscous. Figure 10b shows that B^k is significantly negatively
 530 correlated with τ_s , which is likely due to the similar dependence of P^k and τ_s on $\dot{\gamma}$.

531 Comparing Figures 7 and 8 shows that both Θ^{KS} and B^k are sensitive to θ but exhibit
 532 dissimilar trends despite both being measurements of the partial kinetic stress. The difference
 533 may be attributed to the manner in which they are calculated. Since Θ^{KS} is a depth-averaged
 534 quantity it does not capture the drastic changes in the kinetic pressure profiles which, for
 535 instance, result from formation of plug zones or accumulation of large particles at the flow
 536 surface. These localized effects are better captured by B^k , which is obtained with the functional
 537 form (equation (10)) encoding the effect of the local concentration ϕ_i .

538 4.6 Scaling relationship for the segregation velocity

539 The segregation velocity $w_{p,i}$ measures how fast segregating particles move away from
 540 each other. Recently, scaling relationships for $w_{p,i}$ have been used to highlight the mechanisms
 541 relevant to segregation in different geometries and under different flow conditions, where data
 542 points ideally collapse onto a single curve when normalized by appropriate functional forms.
 543 Likewise, determining the appropriate scaling relationship for $w_{p,i}$ in different flow regimes
 544 encountered here will ideally shed light on the primary mechanisms of segregation in the
 545 presence of ambient fluids.

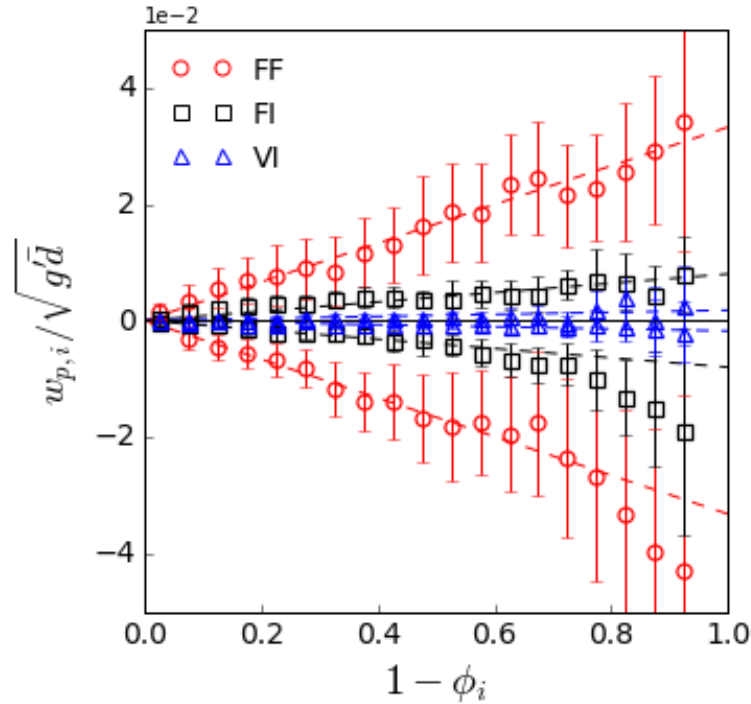


Figure 11. Dimensionless segregation velocities of large and small particles for each flow regime (averaged over all θ) as a function of $1 - \phi_i$.

546 The mean dimensionless segregation velocities for each regime is plotted as a function of
547 $1 - \phi_i$ in Figure 11. Note that the data points (and error bars) represent the means (and standard
548 deviations), obtained from each regime, averaging over all cases with varying θ . Although in
549 each regime the slope of the curves depends slightly on θ (consistent with the trend in Figure
550 4c), the variation is negligible when comparing them across flow regimes (raw data prior to
551 averaging are presented in Appendix D). Figure 11 shows that $w_{p,S}$ and $w_{p,L}$ increase
552 significantly in magnitude across the three flow regimes, and in each regime the segregation
553 velocity depends linearly on $1 - \phi_i$. The slopes of the linear fit are equal in magnitude for both
554 large and small particles. Recently, Jones et al. (2018) have shown that the dependence of $w_{p,i}$
555 on $1 - \phi_i$ can be better described using a quadratic equation which further takes into account the
556 asymmetric dependence of $w_{p,i}$ on the local concentration. The same asymmetry is observed in

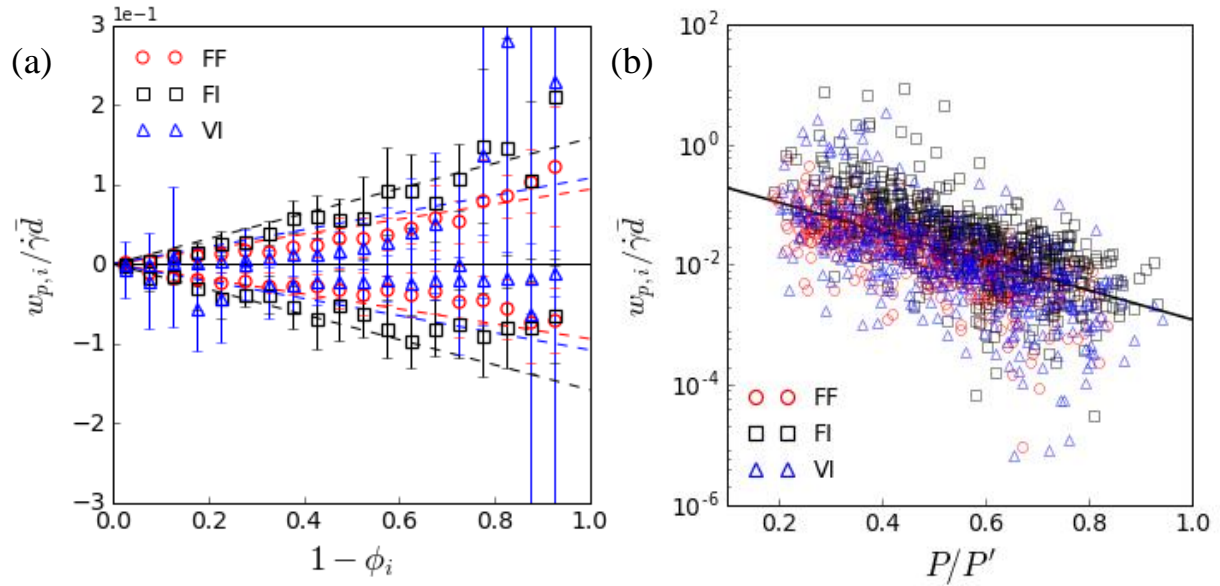


Figure 12. (a) Segregation velocities normalized by local shear rates vs. $1 - \phi_i$. Dashed lines are obtained using a linear fit. (b) The same normalized velocities versus the local total normal stress normalized by the reduced pressure $P' = \Phi(\rho_G - \rho_F)gH \cos \theta$. The fitting line is an exponential function $y = 0.3e^{-5.8x}$.

557 Figure 11 where $w_{p,S}$ is indeed greater than $w_{p,L}$, especially at higher $1 - \phi_i$, indicating that
 558 small particles, in the presence of more large particles, sink faster compared to the rise of large
 559 particles surrounded by the opposite size species. In this study, a simple linear dependence is
 560 nevertheless adopted as it is sufficient to illustrate the fluid effects on $w_{p,i}$ across the different
 561 flow regimes.

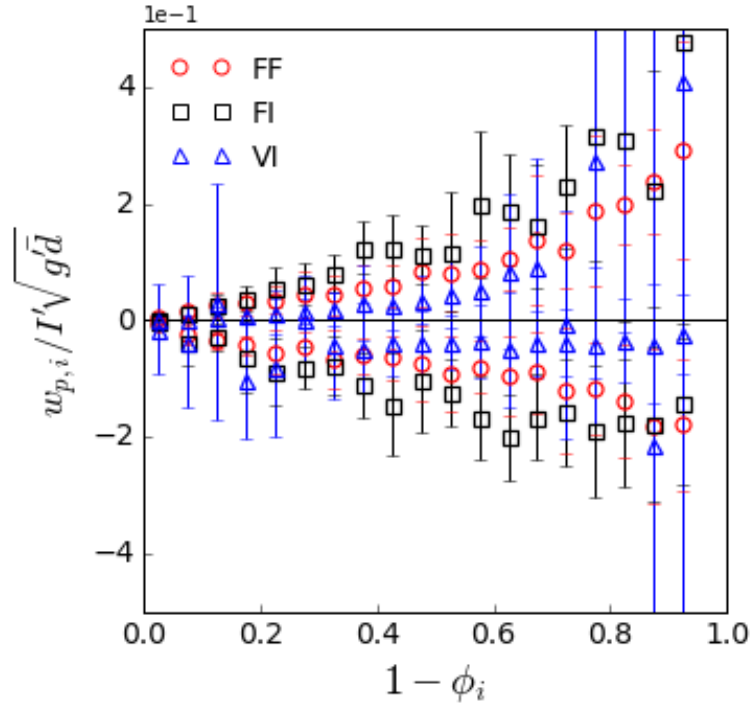


Figure 13. The segregation velocity of large particles for different flow regimes (averaged over all θ) normalized by the reduced inertial number I' .

562 The slopes in the two saturated regimes (FI and VI) are generally lower than that in FF.
 563 Normalizing $w_{p,i}$ by $\dot{\gamma}\bar{d}$, as shown in Figure 12a, drastically changes the slopes of the curves,
 564 largely collapsing the data from different regimes. To see whether the collapse can be further
 565 improved, we check for pressure dependence by plotting the logarithm of the normalized
 566 segregation velocity $w_{p,i}/\dot{\gamma}\bar{d}$ against the dimensionless total pressure $P/\Phi(\rho_G - \rho_F)gH \cos \theta$ as
 567 shown in Figure 12b. The local segregation velocities from different flow regimes show a slight
 568 negative correlation with the normalized pressure. The significant scattering is perhaps due to the
 569 exclusion of local concentrations.

570 The results presented thus far show that the most obvious effects of fluid on segregation
 571 are manifested through the reduction of the shear rates and the pressure. Fluid viscosity is not
 572 found to have any direct effect on the upward and downward percolation of particles and only

573 works to provide more viscous dissipation in the flow direction, thus further decreasing the shear
 574 rate and the kinetic pressure. We summarize these effects by proposing a slight modification to
 575 the scaling relationship by Fry et al. (2018):

$$w_{p,i}/\sqrt{g'\bar{d}} = \pm AI'(1 - \phi_i) \quad (13)$$

576 where $I' = \dot{\gamma}\bar{d}\sqrt{\rho_G/P'}$ is the reduced inertial number and $P' = \Phi(\rho_G - \rho_F)(H - z)g \cos \theta$ is
 577 the reduced pressure which takes into account the effect of buoyancy. A is a dimensionless
 578 proportionality constant which may be dependent on the size ratio and relative concentration of
 579 size species. The signs represent the direction of the percolation.

580 In Figure 13, the mean dimensionless segregation velocities for both large and small
 581 particles are scaled using the reduced inertial number I' and are plotted against $1 - \phi_i$. There is
 582 very little change from the trends shown in Figures 12a, which means that the additional
 583 consideration of the pressure has a limited effect on the scaling of the segregation velocity. We
 584 have attempted to use other functional forms which quantify the rheology of granular-fluid
 585 mixtures, such as the viscous number I_v (Cassar et al., 2013) and viscous-inertial numbers
 586 proposed by Trulsson et al. (2012) and Amarsid et al. (2017), instead of I' , but find very little
 587 improvement with the scaling.

588 **5 Discussion**

589 **5.1 Size segregation in solid-fluid mixtures**

590 Our simulations show that segregation in solid-fluid mixtures are slower and weaker
 591 (related to the degree of segregation α) than when the interstitial fluid is negligible. These results
 592 are qualitatively consistent with experiments conducted using chute flows (Vallance & Savage,

593 2000; Zanuttigh & Ghilardi, 2010). In simulated saturated flows, however, it is observed that the
594 time it takes to segregate increases as the inclination is increased, contrary to what is observed in
595 dry flows. The ambient fluid exerts a drag force in the flow direction counter to the motion of the
596 granular flow, which leads to the formation of a plug zone near the flow surface, corresponding
597 to a region of very low shear rates, thereby slowing down segregation. The only solid-fluid
598 interaction that is significant along the normal direction is the buoyant force; normal drag forces
599 are negligible regardless of the viscosity of the ambient fluid.

600 Evaluating normal volume-averaged forces acting on the rising large particles shows that
601 the main force opposing gravity is the partial contact stress gradient, implying that such gradients
602 drive the large particles up. The buoyancy provided by the ambient fluid reduces inter-particle
603 contacts but at the same time helps support the weight of the rising particles, and effectively
604 works as a scaling factor for the bulk weight. The work of Thornton et al. (2006) shows that this
605 buoyant effect results from the relative densities of the solid and fluid phases such that the closer
606 the densities of the two phases the weaker the segregation. The chute flow experiments of
607 Vallance and Savage (2000) also show that the effect of the relative densities are more
608 significant than that of viscosity. Although this work does not explore the effect of fluid
609 properties in great detail, it can be seen that having similar fluid densities between the FI and VI
610 regimes results in approximately equal partial pressure gradients despite very different ambient
611 fluid viscosities.

612 However, although contact stress partitioning captures the first-order effect of buoyancy
613 across flow regimes, it fails to describe the detailed dependence of the segregation time scale on
614 the inclination angle (i.e., local shear rates). Neither the depth-averaged contact stress gradient
615 Θ^{CS} nor the contact stress partitioning coefficient B^c show clear correlation with τ_s . These results

616 imply that although particle contacts indeed drive the large particles upward, as supported also
617 by recent force measurement research (Guillard et al., 2016; van der Vaart et al., 2018), the
618 method by which it is measured does not account for the dependence of segregation on θ and the
619 rheology that develops therein. Indeed, contact stress partitioning (detailed in Appendix C) relies
620 heavily on the underlying assumption of how forces are split at large-small particle contacts.
621 Future research dedicated to more objective stress partitioning is warranted.

622 The kinetic stress partition B^k on the other hand clearly changes with inclination and
623 correlates better with the segregation rate trends in Figure 4c. Staron and Phillips (2014) have
624 shown that in dry bi-disperse mixtures B^k linearly changes with the shear rate. The segregation
625 timescale in turn decreases with shear rate, leading to the conclusion that greater B^k results in
626 lower τ_s (Staron & Phillips, 2015). A similar correlation is observed in our results (Figure 9b). It
627 is also consistent with previous results that the segregation rate correlates with the velocity
628 difference between layers (Fan & Hill, 2011a, 2011b; Itoh & Hatano, 2019) and that large
629 particles in chute flows are segregated towards the ‘cooler’ regions (near the free surface) of the
630 flow (Dahl & Hrenya, 2004; Staron, & Phillips, 2014).

631 The lower B^k in the fluid saturated regimes indicates the effect of the ambient fluid in
632 decreasing the shear rate and kinetic pressures. The decrease of B^k with inclination in the FI and
633 VI regimes are possibly related to the formation of plug zones near the free surface (occupying
634 about half of the total flow height) as shown in Figure 6. Physically, it can be reasoned that as
635 the motion of large particles are partly driven by the shearing it experiences as it travels between
636 flowing layers (Jing et al., 2017; Staron, 2018), the absence of a defined velocity gradient in the
637 plug zone hinders their upward rise. In light of kinetic sieving, low $\dot{\gamma}$ also implies reduced
638 generation of random voids (Drahn & Bridgwater, 1983), which, when coupled with the

639 reduced energetic motion, decreases the probability of small particles to fit into the available
640 voids, leading to an overall reduction in the downward percolation velocity of small particles.

641 5.2 Implications for saturated mass flows

642 Size segregation, particularly inverse grading, is a common feature in geophysical flows
643 though the extent to which it is observed varies from case to case. Field investigations and
644 physical experiments show that inverse grading is less evident in highly saturated flows which
645 suggests that solid-fluid interactions significantly affect particle dynamics (Major & Pierson,
646 1992; Zhou et al., 2019). This work only focuses on the case where the granular flows are dense
647 and completely saturated. Granular flows are simulated according to the rheology that arises
648 from solid-fluid interactions defined by the different flow regimes, instead of simply varying the
649 fluid material properties; indeed, larger particles flowing in an ambient viscous fluid may behave
650 like a fluid-inertial flow, while very fine particles flowing in water can fall into the viscous
651 regime (Cassar et al., 2005; Jing et al., 2019). The findings imply that the degree of inverse
652 grading observed in the deposits of geophysical mass flows can be used to evaluate the dominant
653 transport mechanism during the course of its motion. This can be particularly useful in
654 evaluating mass flow events which have completely dried up and whose previous state of
655 saturation cannot be judged accurately. Evident inverse grading means that the flow is inertial,
656 dominated by frictional-collisional interactions with minimal involvement from interstitial fluid.
657 This can either mean that the interstitial fluid is not very viscous, is significantly less dense than
658 the solid particles, or that the flowing particles are significantly large and massive. Consistently,
659 inertial flows of dissimilarly sized granular mixtures result in efficient levee formation (Félix &
660 Thomas, 2004; de Haas et al., 2015). On the other hand, poor inverse grading in the deposits
661 would imply that the flow is viscous, which means that viscous dissipation is dominant and

662 segregation develops very slowly. Such flows usually involve very viscous slurries with high
663 fines content and often correspond to poor levee formation (Zhou et al., 2019).

664 Segregation is considered to be a transient process and hence in geophysical flow models,
665 which take size segregation into account, it is often assumed that size separation is fully-
666 developed, i.e. small and large particles have completely separated. The presence of ambient
667 fluids however results in longer segregation times, such that the mixture may still be well mixed
668 during the entire duration of the flow. This may have implications in modelling levee formation
669 (Baker et al., 2016) and breaking size segregation waves (van der Vaart et al., 2018) since such
670 features require the large particles to be at the free surface for them to be easily and efficiently
671 transported to the front or lateral sides of the flow. Lastly, the state of mixing and segregation in
672 granular-fluid flows also have implications on its internal friction (Rognon et al., 2007;
673 Yohannes & Hill, 2010; Tripathi & Khakhar, 2011).

674 **6 Concluding remarks**

675 Size segregation in saturated granular flows are studied using the numerical fluid-
676 granular simulations. Granular flows are modelled according to three granular-fluid flow regimes
677 – free-fall, fluid inertial, and viscous – where each regime exhibits distinct flow dynamics in
678 which different rates of segregation are observed. It is found that, consistent with experiments,
679 the presence of a viscous fluid effectively diminishes the degree of separation and slows down
680 segregation.

681 Through detailed evaluation of different forcing terms in the momentum equation of the
682 mixture theory of segregation, we find that the ambient fluid reduces segregation first by
683 reducing the contact stress gradients through buoyant effects. The ambient fluid also slows down

684 segregation by reducing the shear rate, partly by inducing the formation of plug zones near the
685 free surface where velocity gradients are greatly inhibited. This subtle dependence of segregation
686 on rheology is reflected by kinetic stress partitioning, but not contact stress partitioning (likely
687 because force splitting in the current partitioning method does not depend on flow information).
688 The drag force in the normal direction does not directly hinder the upward rise of large particles
689 regardless of the viscosity of the ambient fluid. The segregation velocity is therefore independent
690 of viscosity and can be mainly written as a function of the flow shear rates and reduced pressures
691 expressed in the form of a reduced inertial number.

692 The current work is an attempt to further understand the particle dynamics which develop
693 under the influence of fluid interactions. A more detailed evaluation of the effects of viscosity
694 and the relative density, in which the flow rheology is isolated, is warranted for better
695 understanding the factors affecting segregation in solid-fluid mixture flows. It should also be
696 noted that the system presented in this paper is somewhat different from actual granular-fluid
697 chute flows in which the fluid phase flows along with (or independently from) the solid phase,
698 though the segregation and rheology presented here are qualitatively consistent with such
699 systems. Different fluid boundary conditions, such as periodic boundaries, may result in subtle
700 differences in the segregation mechanisms. Nevertheless, the fluid effects determined in the
701 study (i.e., buoyancy and reduced shear rates) are expected to be valid regardless of the boundary
702 conditions and therefore are relevant to a wide range of fluid-granular flow scenarios.

703 **A: The CFD-DEM method**

704 The DEM and CFD modules are implemented using the open-source C++ libraries ESyS
705 Particle (Weatherley et al., 2014) and OpenFOAM, respectively. The coupling between CFD and

706 DEM relies on a message passing algorithm that exchanges information between the DEM and
 707 the CFD through a dynamic linked library in which interaction forces are solved at fixed time
 708 intervals (Zhao, 2017).

709 In the DEM, the translational and rotational displacements of particles are calculated
 710 based on Newton's second law of motion and are updated after each numerical timestep. The
 711 governing equations can be written as:

$$m_j \frac{d^2 \mathbf{x}_j}{dt^2} = \sum_c (\mathbf{f}_{nc} + \mathbf{f}_{tc}) + m_j \mathbf{g} + \mathbf{F}_j^{F-G} \quad (14)$$

$$\mathbf{I}_j \frac{d\boldsymbol{\omega}_j}{dt} = \sum_c \mathbf{r}_c \times \mathbf{f}_{tc} \quad (15)$$

712 Here, m_j and \mathbf{x}_j are the mass and position of a particle j at a single numerical time-step, \mathbf{I}_j is the
 713 moment of inertia of a sphere, $\boldsymbol{\omega}_j$ is the rotational acceleration, and \mathbf{r}_c is the distance between
 714 the centers of two contacting spheres. \mathbf{f}_{nc} and \mathbf{f}_{tc} are the normal and tangential forces of
 715 particle-particle interactions defined at a contact point c , and are calculated according to the
 716 spring-dashpot model of Cundall & Strack, (1979):

$$\mathbf{f}_{nc} = K_n \delta_n \mathbf{n}_c + C_n \quad (16)$$

$$\mathbf{f}_{tc} = \min\{\mathbf{f}_{tc}^{t-1} + K_t \Delta \mathbf{v}_c^t, \mu \mathbf{f}_{nc}\} \quad (17)$$

717 where $K_n = \pi E (r_1 + r_2) / 4$ and $K_t = \pi E (r_1 + r_2) / 8(1 + G)$ are the particle normal and shear
 718 stiffness where E is Young's modulus, G is Poisson's ratio, and r_1 and r_2 are the radii of the
 719 contacting particles. δ_n is the overlapping distance between the two particles, $\Delta \mathbf{v}_c$ is the relative
 720 velocity of the contacting particles, and \mathbf{n}_c is the unit vector of the contact normal. The damping
 721 force $C_n = 2\Omega \sqrt{K_n (m_1 + m_2) / 2}$ is used to replicate the energy dissipation induced by plastic

722 deformation and shearing due to particle asperities. Ω is the damping coefficient, an empirical
 723 value related to the coefficient of restitution for collisional velocities. m_1 and m_2 are the masses
 724 of the contacting particles. \mathbf{f}_{tc}^{t-1} and $\Delta\mathbf{v}_c^t$ are the tangential components of the force of the
 725 previous time step and relative contact velocities, respectively. μ is the contact friction
 726 coefficient.

727 The final term on the right hand side of equation (14) is the solid-fluid interaction force
 728 (Zhao, 2017):

$$\mathbf{F}^{F-G} = \mathbf{F}_j^b + \mathbf{F}_j^d = -V_j \nabla P_F + \frac{1}{2} C_d \rho_F \frac{\pi D^2}{4} |\mathbf{U}_F - \mathbf{U}_G| (\mathbf{U}_F - \mathbf{U}_G) \Phi_F^{(1-\chi)} \quad (18)$$

729 As presented in 2.1, \mathbf{F}_j^b is the buoyant force where V_j is the volume of a particle j and ∇P_F is the
 730 fluid pressure gradient. \mathbf{F}_j^d is the drag force which quantifies the force acting opposite to the
 731 relative velocity between the particle and the surrounding fluid. The drag force equation
 732 proposed by Di Felice (1994) is used in this study where:

$$C_d = \frac{24}{Re} (1 + 0.15 Re^{0.681}) + \frac{0.407}{1 + \frac{8710}{Re}} \quad (19)$$

$$Re = \rho_F d |\mathbf{U}_F - \mathbf{U}_G| / \eta_F \quad (20)$$

733 are the drag coefficient and Reynold's number defined at the particle scale, respectively. \mathbf{U}_F
 734 and \mathbf{U}_G are the fluid and particle velocities, ρ_F is the fluid density, and η_F is the dynamic
 735 viscosity. The term $\Phi_F^{(1-\chi)}$ is an empirical relationship introduced to express the influence of
 736 particle concentration on the drag coefficient where $\chi = 3.7 - 0.65 \exp\left[-\frac{(1.5 - \log_{10} Re)^2}{2}\right]$. The
 737 form of the drag law presented in equation (19) is chosen for its ability to correctly model the
 738 drag coefficient for a wide range of Re (Zhao, 2017).

739 The fluid domain is discretized into three-dimensional cells where the Navier-Stokes
 740 equations are solved using the Finite Volume Method (FVM) (Anderson, 1995). The mass and
 741 momentum continuum equations are written as:

$$\frac{\partial(\Phi_F \rho_F)}{\partial t} + \nabla \cdot (\Phi_F \rho_F \mathbf{U}_F) = 0 \quad (21)$$

$$\frac{\partial(\Phi_F \rho_F \mathbf{U}_F)}{\partial t} + \nabla \cdot (\Phi_F \rho_F \mathbf{U}_F \otimes \mathbf{U}_F) - \Phi_F \nabla \cdot \mathbf{S}_F = -\Phi_F \nabla P_F + \Phi_F \rho_F \mathbf{g} + \mathbf{f}_d \quad (22)$$

742 where \mathbf{S}_F is the fluid stress tensor calculated via the standard $k - \varepsilon$ turbulence model (Zhao,
 743 2017). The term $\mathbf{f}_d = \sum_{j=1}^N F_j^d / V_{fc}$ is the drag force per unit fluid volume where V_{fc} is the fluid
 744 cell volume. The fluid pressures and velocities that are calculated in each cell are used, in turn, to
 745 calculate the interaction forces.

746 **B: Averaging method**

747 To calculate the relevant kinematic and rheological properties, the entire flow is divided
 748 into sampling volumes with fixed dimensions $V_M = 35d_s \times 10d_s \times \Delta z$, where $\Delta z = d_L$. These
 749 properties are calculated considering the contribution of the part of each particle that falls within
 750 Δz centered at a height z . For a granular flow with total flow velocity $\mathbf{U}_G = u\hat{x} + v\hat{y} + w\hat{z}$, the
 751 volume fractions Φ_i and streamwise velocities u_i for particles of species i are calculated as (Fan
 752 et al., 2014a; Hill & Tan, 2014):

$$\Phi_i(z) = \frac{\sum_j V_{ij}}{V_M} \quad (23)$$

$$u_i(z) = \frac{\sum_j u_{ij} V_{ij}}{\sum_j V_{ij}} \quad (24)$$

753 respectively. V_{ij} and u_{ij} are the fractional volumes and velocities of a particle j of size species i .
 754 Species local volume concentrations are calculated as $\phi_i = \Phi_i / \sum_{L,S} \Phi_i$. The shear rate is
 755 calculated as the derivative of the time-averaged velocities $\dot{\gamma} = \left| \frac{du}{dz} \right|$. The segregation
 756 velocity is calculated as $w_{p,i} = w_i - w$, where w is the local normal average velocity at z , and
 757 w_i is the local averaged velocity of a particle.

758 The partial kinetic stress tensor is calculated as:

$$\sigma_i^k(z) = \frac{1}{V_M} \sum_j m_{ij} \Lambda_{ij} \otimes \Lambda_{ij} \quad (25)$$

759 where Λ_{ij} is the fluctuating velocity of a particle j of species i , defined as the difference of the
 760 instantaneous and time-averaged velocities, where the latter is calculated as $w(z) =$
 761 $\sum_i (\Phi_i(z) w_i(z)) / \sum_i \Phi_i(z)$. The contact stress tensor is calculated as:

$$\sigma_i^c(z) = \frac{1}{V_M} \left[\sum_{j \neq m} \mathbf{F}_{i,jm} \otimes \mathbf{l}_{i,jm} \right] \quad (26)$$

762 where $\mathbf{F}_{i,jm} = \mathbf{f}_{nc} + \mathbf{f}_{tc}$ is the contact force between particles j and m , where j is a particle
 763 belonging to size species i , and $\mathbf{l}_{i,jm}$ is the distance between their centers,. Assuming that the
 764 normal stress is isotropic in all directions, contact and kinetic partial pressures are calculated as
 765 $P_i^c = \sigma_i^{c,zz}$ and $P_i^k = \sigma_i^{k,zz}$, respectively. Total partial pressure is $P_i = P_i^c + P_i^k$ and bulk
 766 pressure is calculated as $P = P_L + P_S$. Contact and kinetic pressure fractions are calculated
 767 as $\psi_i^c = P_i^c / P^c$ and $\psi_i^k = P_i^k / P^k$, respectively.

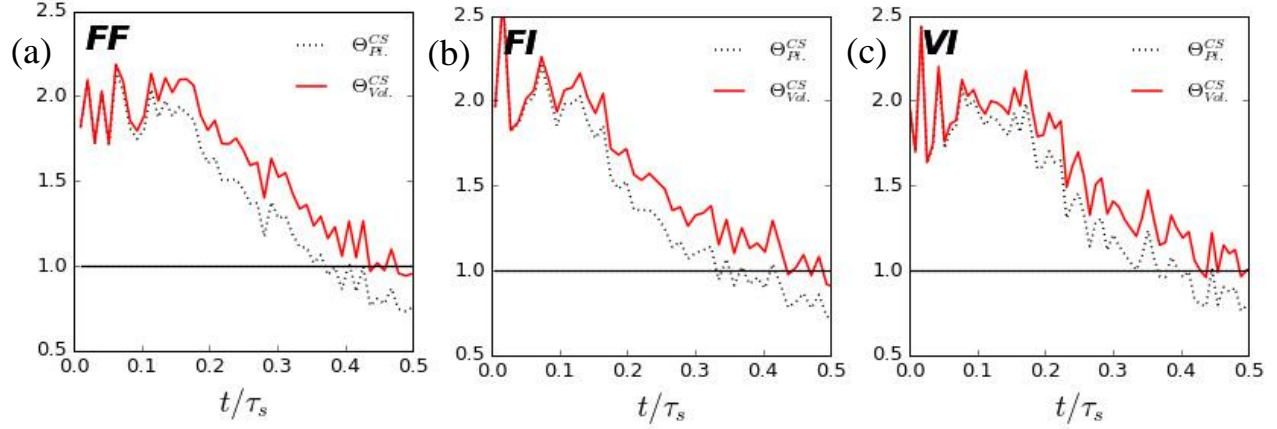


Figure 14. The effect of radius- and volume-based partitioning on the depth-averaged contact stress gradients in the (a) FF, (b) FI, and (c) VI regimes.

768 Data is recorded at every computational time step of 0.1 seconds (10 Hz). Calculation of
 769 relevant parameters are taken at specific time intervals over 20 such time steps. Values
 770 calculated using equations (23)-(26) are smoothed over 10 time intervals centered at a chosen
 771 time step.

772 **C: Contact stress partitioning**

773 The calculation of the contact pressure, the pressure fraction, and partition coefficient are
 774 greatly affected by how the contact forces are partitioned among differently sized constituents.
 775 The conclusions one can make based on the contact stresses can vary depending on the choice of
 776 partitioning function. Here, we briefly discuss the effects of choosing partition forces based on
 777 the relative radius or volume of contacting particles. Contact stresses, for differently sized
 778 particles, partitioned based on the radius ratio (i.e., at the point of contact) are calculated as:

$$\sigma_i^c = \mathbf{F}_{i,LS} \otimes \left(\frac{r_i}{r_L + r_S} \right) \mathbf{l}_{LS} \quad (27)$$

779 where r_i is the radius of the particle specie i . Contact stresses partitioned according to the
 780 volume of contacting particles are calculated as:

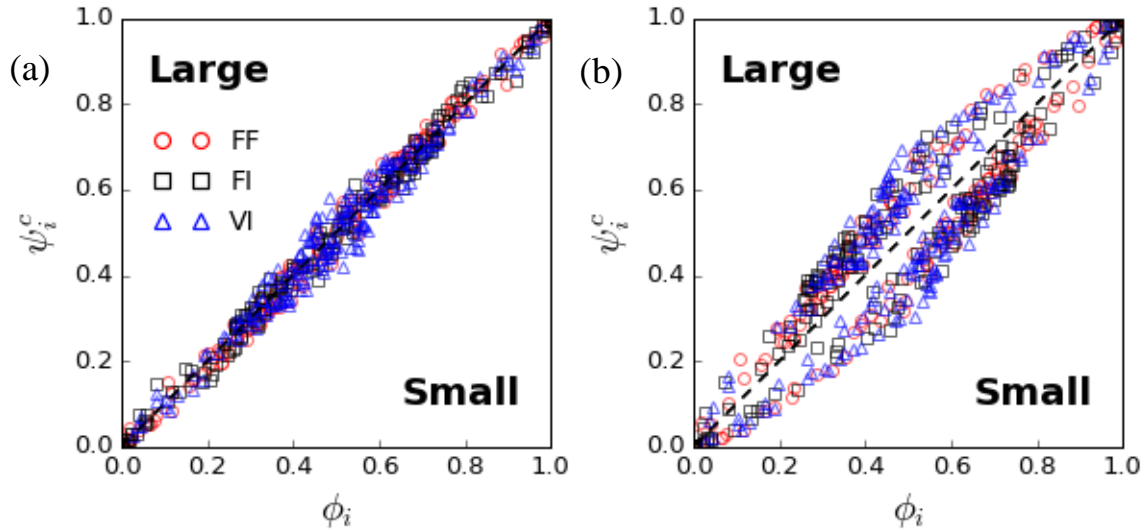


Figure 15. The contact pressure fraction ψ_i^c as a function of the local concentration ϕ_i for mixtures in different regimes flowing at 22° for forces partitioned according to the (a) radii and (b) volumes of contacting particles.

$$\sigma_i^c = F_{i,LS} \otimes \left(\frac{r_i^3}{r_L^3 + r_S^3} \right) \mathbf{l}_{LS} \quad (28)$$

781 As shown in Figure 14, the contact stresses calculated using the radius-based partitioning
 782 are smaller than that the volume-based partitioning, regardless of the flow regime. The two
 783 trends separate as the mixture segregates and the interaction between large and small particles
 784 are maximum. Figure 15 shows that using the contact-point partitioning the contact stress
 785 fraction appears to be equal to the local concentration, such that B^c is very small, implying that
 786 contact stresses do not drive segregation at all and simply work to balance the large particles'
 787 weight (similar to Hill & Tan 2014). On the other hand, partitioning according to the volume of
 788 contacting particles would result in an asymmetry in the contact stresses where the large particles
 789 receive a larger portion which then leads one to infer that contact stresses do in fact drive
 790 segregation. The latter method is considered to be more reasonable, and used in the main text, as
 791 recent segregation force studies showed clearly that rising of large particles is a result of net
 792 contact forces overcoming the particle weight (Guillard et al., 2016; van der Vaart et al., 2018).

793 Besides, a volume-based partitioning function in Tunuguntla et al. (2014) was reported to
 794 produce good prediction of size- and density-segregation.

795 **D: Calculation of c_{PI} and c_D**

796 Solving the momentum equation in the mixture theory requires determination of the
 797 linear drag coefficient c_{PI} and diffusion coefficient c_D . According to Gray and Chugunov (2006),
 798 the diffusion coefficient can be expressed as $c_D = c_{PI}D$, where D is the diffusivity which
 799 measures the ability of a particle to randomly disperse throughout the mixture due to random
 800 collisions. D can be determined independently from the other components of the momentum
 801 equation through the mean squared displacements (MSD) of individual particles $\langle \Delta z(\Delta t)^2 \rangle =$
 802 $2D\Delta t$, where $\Delta z(\Delta t) = z(t_0 + \Delta t) - z(t_0) - \int_{t_0}^{t_0+\Delta t} w(t)dt$ is the non-affine part of the particle
 803 trajectory along the normal direction per unit time, and $\langle x \rangle$ represents ensemble averaging within
 804 a flowing layer (Fan et al., 2014). Using the calculated values, c_D can then be obtained by finding
 805 the corresponding value that will provide the best-fit for the following balance equation (which
 806 assumes steady state):

$$c_{PI} = \frac{\frac{\partial P_i}{\partial z} - \Phi_i \rho_i g}{-\left[\Phi_i \rho_i (w_i - w) + \rho_G D \frac{\partial \Phi_i}{\partial z} \right]} \quad (29)$$

807 The determined c_{PI} value is then multiplied by D to calculate the diffusion coefficient c_D .

808 **E: Formation of plug zones**

809 As particles move within an ambient fluid they experience a drag force F^d which
 810 counteracts the flow. Although there are two fluid forces considered here, it is only F^d which
 811 works opposite to the flow direction. Figures 16a and 16b show the drag force F^d along the

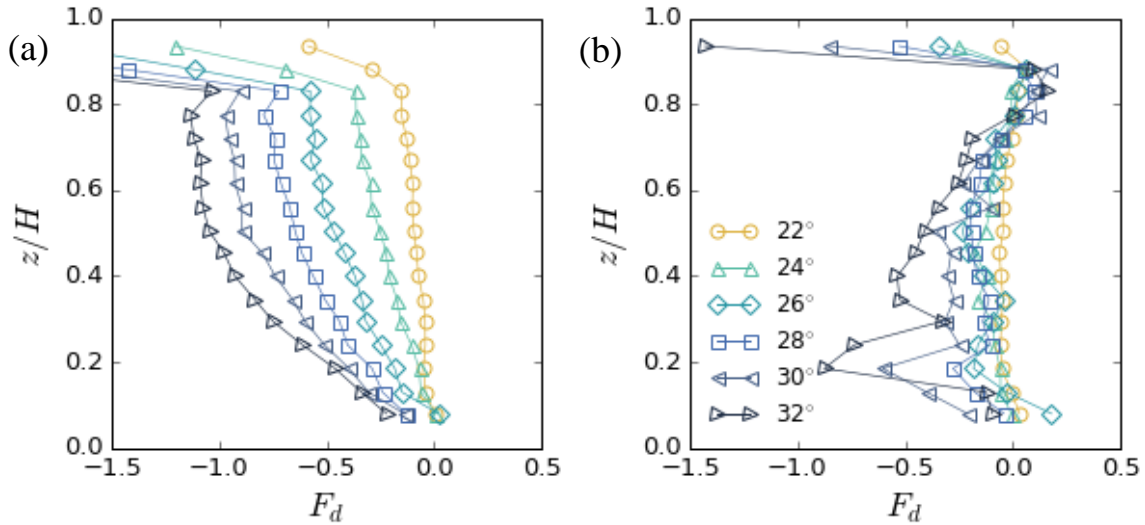


Figure 16. Dimensionless drag force F_d in the flow direction in the (a) FI and (b) VI regimes.

812 stream-wise direction in the FI and VI regimes, respectively, normalized by the buoyant weight
 813 (averaged over $t = 0.1 \sim 0.5\tau_s$). As calculated from equation (18), F^d is negative when the solid
 814 phase flows faster than the fluid phase. F^d in FI becomes increasingly negative with θ and is
 815 highest near the free surface. This increasing resistive force leads to the formation of plug zones
 816 in the u profiles of FI. The abrupt increase at the topmost part is due to the low fluid flow
 817 velocity at the boundary of the fluid and mixture free surface. The F^d in the VI are surprisingly
 818 lower than in FI despite being more viscous mainly because the relative velocities between the
 819 solid and fluid phases are low. For $\theta = 22^\circ \sim 26^\circ$, F^d in VI does not significantly increase
 820 (negatively) and only appears to fluctuate around 0. F^d slightly increases at the higher angles
 821 $\theta = 28^\circ \sim 32^\circ$, manifested through large fluctuations within the flow body.

822 **F: Segregation velocities in different flow regimes**

823 Figure 17 shows raw segregation velocities $w_{p,i}$ for varying slope angles in each flow
 824 regime. Data in each regime practically follow the same trend and can therefore be taken as a
 825 single data set. There are subtle differences in the fitted slopes between samples at different θ but

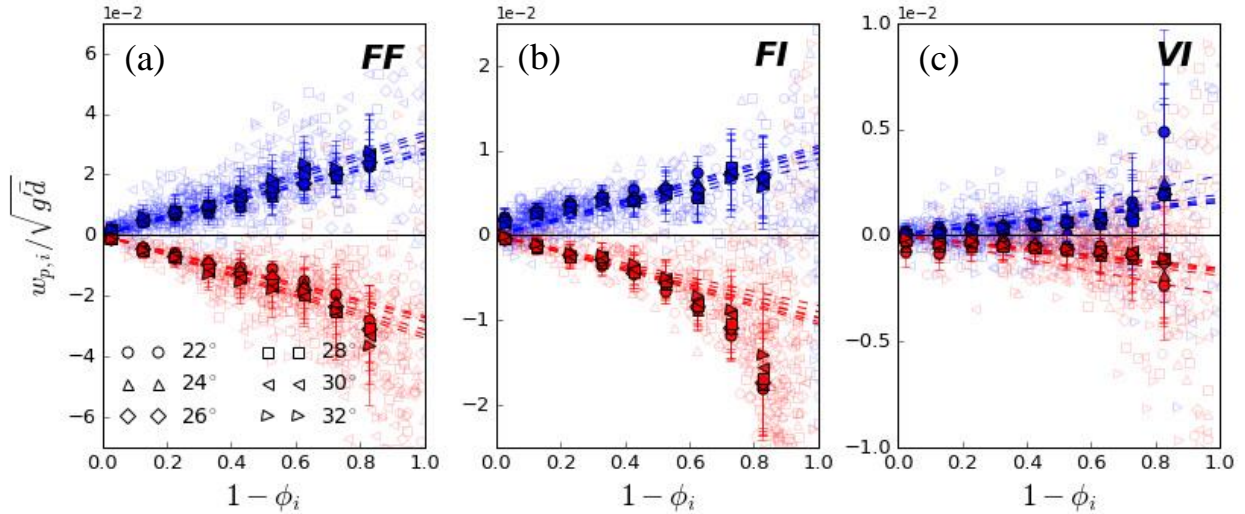


Figure 17. The normalized segregation velocities $w_{p,i}$ for every θ in (a) FF, (b) FI, and (c) VI. The solid markers indicate the mean $w_{p,i}$ and the background markers are the raw data. Blue markers represent $w_{p,i}$ for large particles and red markers are for the small particles. The dashed lines are the slopes of the mean $w_{p,i}$; the small and large particles have equal slopes but different signs.

826 are much lower than the differences between flow regimes. The solid symbols are the mean $w_{p,i}$
 827 averaged over $1 - \phi_i = 0.1$ while the lightly shaded symbols are all the $w_{p,i}$ for all values of θ .

828 Acknowledgments

829 The authors acknowledge financial support from the National Natural Science
 830 Foundation of China (grant nos. 41941017, 11672318), Key Research Program of Frontier
 831 Sciences, Chinese Academy of Sciences (CAS) (grant no. QYZDB-SSW-DQC010), and the
 832 CAS-TWAS President's Fellowship for International PhD students. Data and codes that can be
 833 used to replicate and validate the results presented here are available through the following link:
 834 <http://doi.org/10.5281/zenodo.3663215>.

835 References

836 Amarsid, L., Delenne, J. Y., Mutabaruka, P., Monerie, Y., Perales, F., & Radjai, F. (2017).

- 837 Viscoinertial regime of immersed granular flows. *Physical Review E*, 96(1).
838 doi:10.1103/PhysRevE.96.012901
- 839 Anderson, J.D. (1995). Computational fluid dynamics: The basics with applications. McGraw-Hill
- 840 Bagnold, R. A. (1954). Experiments on a Gravity-free Dispersion of Large Solid Spheres in a
841 Newtonian Fluid under Shear. *Proceedings of the Royal Society A*, 225(1160), 49–63.
- 842 Baker, J., Gray, J. M. N. T., & Kokelaar, B. P. (2016). Particle Size-Segregation and
843 Spontaneous Levee Formation in Geophysical Granular Flows. *International Journal of*
844 *Erosion*, 9(4), 174–178.
- 845 Baker, J. L., Johnson, C. G., & Gray, J. M. N. T. (2016). Segregation-induced finger formation in
846 granular free-surface flows. *Journal of Fluid Mechanics*, 809, 168–212.
847 doi:10.1017/jfm.2016.673
- 848 Cassar, C., Nicolas, M., & Pouliquen, O. (2005). Submarine granular flows down inclined
849 planes. *Physics of Fluids*, 17(10). doi:10.1063/1.2069864
- 850 Courrech du Pont, S., Gondret, P., Perrin, B., & Rabaud, M. (2003). Granular Avalanches in
851 Fluids. *Physical Review Letters*, 90(4), doi:10.1103/PhysRevLett.90.044301
- 852 Coussot, P., & Meunier, M. (1996). Recognition, classification and mechanical description of
853 debris flows. *Earth-Science Reviews*, 40(3–4), 209–227, doi:10.1016/0012-8252(95)00065-
854 8
- 855 Cundall, P. A., & Strack, O. D. L. (1979). A discrete numerical model for granular assemblies.
856 *Géotechnique*, 29(1), 47–65, doi: 10.1680/geot.1979.29.1.47
- 857 Dahl, S. R., & Hrenya, C. M. (2004). Size segregation in rapid, granular flows with continuous
858 size distributions. *Physics of Fluids*, 16(1), 1–13. doi:10.1063/1.1626682
- 859 De Haas, T., Braat, L., Leuven, J. R. F. W., Lokhorst, I. R., & Kleinhans, M. G. (2015). Effects
860 of debris flow composition on runout, depositional mechanisms, and deposit morphology in
861 laboratory experiments. *Journal of Geophysical Research F: Earth Surface*, 120(9), 1949–
862 1972. doi:10.1002/2015JF003525
- 863 Drahn, J. A., & Bridgwater, J. (1983). The mechanisms of free surface segregation. *Powder*
864 *Technology*, 36(1), 39–53. doi:10.1016/0032-5910(83)80007-2
- 865 Fan, Y., & Hill, K. M. (2011a). Phase transitions in shear-induced segregation of granular
866 materials. *Physical Review Letters*, 106(21), doi:10.1103/PhysRevLett.106.218301
- 867 Fan, Y., & Hill, K. M. (2011b). Theory for shear-induced segregation of dense granular
868 mixtures. *New Journal of Physics*, 13. doi:10.1088/1367-2630/13/9/095009
- 869 Fan, Y., Schlick, C. P., Umbanhowar, P. B., Ottino, J. M., & Lueptow, R. M. (2014). Modelling
870 size segregation of granular materials: The roles of segregation, advection and diffusion.

- 871 *Journal of Fluid Mechanics*, 741, 252–279. doi:10.1017/jfm.2013.680
- 872 Félix, G., & Thomas, N. (2004). Relation between dry granular flow regimes and morphology of
873 deposits: Formation of levées in pyroclastic deposits. *Earth and Planetary Science Letters*,
874 221(1–4), 197–213. doi:10.1016/S0012-821X(04)00111-6
- 875 Ferdowsi, B., Ortiz, C. P., Houssais, M., & Jerolmack, D. J. (2017). River bed armoring as a
876 granular segregation phenomenon. *Nature Communications*, 8(1363), 10.
877 doi:10.1038/s41467-017-01681-3
- 878 Fry, A. M., Umbanhowar, P. B., Ottino, J. M., & Lueptow, R. M. (2018). Effect of pressure on
879 segregation in granular shear flows. *Physical Review E*, 97(6), 062906.
880 <https://doi.org/10.1103/PhysRevE.97.062906>
- 881 Gajjar, P., & Gray, J. M. N. T. (2014). Asymmetric flux models for particle-size segregation in
882 granular avalanches. *Journal of Fluid Mechanics*, 757, 297–329. doi:10.1017/jfm.2014.503
- 883 Gray, J. M.N.T., & Chugunov, V. A. (2006). Particle-size segregation and diffusive remixing in
884 shallow granular avalanches. *Journal of Fluid Mechanics*, 569,
885 doi:10.1017/S0022112006002977
- 886 Gray, J. M.N.T., & Ancy, C. (2009). Segregation, recirculation and deposition of coarse
887 particles near two-dimensional avalanche fronts. *Journal of Fluid Mechanics*, 629, 387–
888 423. doi:10.1017/S0022112009006466
- 889 Gray, J.M.N.T. (2018). Particle Segregation in Dense Granular Flows. *Annu. Rev. Fluid Mech*,
890 50, 407–433. doi:10.1146/annurev-fluid-122316
- 891 Gray, J.M.N.T., & Thornton, A.R. (2005). A theory for particle size segregation in shallow
892 granular free-surface flows. *Proceedings of the Royal Society A*, 461, 1447–1473.
893 doi:10.1098/rspa.2004.1420
- 894 Guillard, F., Forterre, Y., & Pouliquen, O. (2016a). Scaling laws for segregation forces in dense
895 sheared granular flows. *Journal of Fluid Mechanics*, 807, doi:10.1017/jfm.2016.605
- 896 Hill, K. M., & Tan, D. S. (2014). Segregation in dense sheared flows: Gravity, temperature
897 gradients, and stress partitioning. *Journal of Fluid Mechanics*, 756, 54–88.
898 doi:10.1017/jfm.2014.271
- 899 Ilstad, T., Elverhoi, A., Issler, D., & Marr, J.G. (2004). Subaqueous debris flow behaviour and its
900 dependence on the sand/clay ratio : a laboratory study using particle tracking. *Marine*
901 *Geology*, 213, 415–438. doi:10.1016/j.margeo.2004.10.017
- 902 Itoh, R., & Hatano, T. (2019). Geological implication of grain-size segregation in dense granular
903 matter. *Philosophical Transactions of the Royal Society A: Mathematical, Physical and*
904 *Engineering Sciences*, 377(2136). doi:10.1098/rsta.2017.0390
- 905 Iverson, R. M. (1997). The Physics of Debris Flows. *Reviews of Geophysics*, 35(3), 245–296,

- 906 doi:10.1029/97RG00426
- 907 Jing, L., Kwok, C. Y., & Leung, Y. F. (2017). Micromechanical Origin of Particle Size
908 Segregation. *Physical Review Letters*, *118*(11).
909 <https://doi.org/10.1103/PhysRevLett.118.118001>
- 910 Jing, L., Yang, G. C., Kwok, C. Y., & Sobral, Y. D. (2019). Flow regimes and dynamic
911 similarity of immersed granular collapse : A CFD-DEM investigation. *Powder Technology*,
912 *345*, 532–543. <https://doi.org/10.1016/j.powtec.2019.01.029>
- 913 Johnson, C. G., Kokelaar, B. P., Iverson, R. M., Logan, M., Lahusen, R. G., & Gray, J. M. N. T.
914 (2012). Grain-size segregation and levee formation in geophysical mass flows. *Journal of*
915 *Geophysical Research*, (March). <https://doi.org/10.1029/2011JF002185>
- 916 Jones, R.P., Isner, A.B., Xiao, H.Y., Ottino, J.M., Umbanhowar, P.B., & Lueptow, R.M. (2018).
917 Asymmetric dependence of segregation fluxes in granular flows. *Physical Review Fluids*,
918 *3*(9), <http://doi.org/10.1103/PhysRevFluids.3.094304>.
- 919 Kleinhans, M. G. (2004). Sorting in grain flows at the lee side of dunes. *Earth-Science Reviews*,
920 *65*, 75–102. [https://doi.org/10.1016/S0012-8252\(03\)00081-3](https://doi.org/10.1016/S0012-8252(03)00081-3)
- 921 Kokelaar, B. P., Graham, R. L., Gray, J. M. N. T., & Vallance, J. W. (2014). Fine-grained linings
922 of leveed channels facilitate runout of granular flows. *Earth and Planetary Science Letters*,
923 *385*, 172–180. <https://doi.org/10.1016/j.epsl.2013.10.043>
- 924 Lai, Z., Vallejo, L. E., Zhou, W., Ma, G., Espitia, J. M., Caicedo, B., & Chang, X. (2017).
925 Collapse of granular columns with fractal particle size distribution: implications for
926 understanding the role of small particles in granular flows. *Geophysical Research Letters*,
927 *44*(24), 12,181–12,189. <https://doi.org/10.1002/2017GL075689>
- 928 Linares-Guerrero, E., Goujon, C., & Zenit, R. (2007). Increased mobility of bidisperse granular
929 avalanches. *Journal of Fluid Mechanics*, *593*, 475–504.
930 <https://doi.org/10.1017/S0022112007008932>
- 931 Mainali, A., & Rajaratnam, N. (1994). Experimental Study of Debris Flows. *Journal of*
932 *Hydraulic Engineering*, *120*(1), 104–123.
- 933 Major, J. J., & Pierson, T. C. (1992). Debris flow rheology: Experimental analysis of fine-
934 grained slurries. *Water Resources Research*, *28*(3), 841–857, doi:10.1029/91WR02834
- 935 Mandal, S., & Khakhar, D. V. (2019). Dense granular flow of mixtures of spheres and dumbbells
936 down a rough inclined plane: Segregation and rheology. *Physics of Fluids*, *31*(2),
937 doi:10.1063/1.5082355
- 938 May, L. B. H., Golick, L. A., Phillips, K. C., Shearer, M., & Daniels, K. E. (2010). Shear-driven
939 size segregation of granular materials: Modeling and experiment. *Physical Review E*, *81*(5),
940 2–9, doi:10.1103/PhysRevE.81.051301

- 941 Midi, G. D. R. (2004). On dense granular flows. *European Physical Journal E*, *14*(4), 341–365.
942 doi:10.1140/epje/i2003-10153-0
- 943 Mulder, T., & Alexander, J. (2001a). The physical character of subaqueous sedimentary density
944 flow and their deposits. *Sedimentology*, *48*(2), 269–299. doi:10.1046/j.1365-
945 3091.2001.00360.x
- 946 Rognon, P. G., Roux, J. N., Naaim, M., & Chevoir, F. (2007). Dense flows of bidisperse
947 assemblies of disks down an inclined plane. *Physics of Fluids*, *19*(5), 7–11.
948 doi:10.1063/1.2722242
- 949 Savage, S. B., & Hutter, K. (1989). The motion of a finite mass of granular material down a
950 rough incline. *Journal of Fluid Mechanics*, *199*(2697), 177–215,
951 doi:10.1017/S0022112089000340
- 952 Savage, S. B., & Lun, C. K. K. (1988). Particle size segregation in inclined chute flow of dry
953 cohesionless granular solids. *Journal of Fluid Mechanics*, *189*, 311–335,
954 doi:10.1017/S002211208800103X
- 955 Schlick, C. P., Fan, Y., Isner, A. B., Umbanhowar, P. B., Ottino, J. M., & Lueptow, R. M.
956 (2015). Modeling Segregation of bidisperse granular materials using physical control
957 parameters in the quasi-2D bounded heap. *Journal of the American Institute of Chemical*
958 *Engineers*, *61*(5). doi:10.1002/aic.14780
- 959 Siman-Tov, S., & Brodsky, E. E. (2018). Gravity-Independent Grain Size Segregation in
960 Experimental Granular Shear Flows as a Mechanism of Layer Formation. *Geophysical*
961 *Research Letters*, *45*(16), 8136–8144, doi:10.1029/2018GL078486
- 962 Staron, L., & Phillips, J. C. (2014). Segregation time-scale in bi-disperse granular flows. *Physics*
963 *of Fluids*, *26*(3), doi:10.1063/1.4867253
- 964 Staron, L., & Phillips, J. C. (2015). Stress partition and microstructure in size-segregating
965 granular flows, *022210*, 1–8, doi:10.1103/PhysRevE.92.022210
- 966 Staron, L. (2018). Rising dynamics and lift effect in dense segregating granular flows. *Physics of*
967 *Fluids*, *30*(12). doi:10.1063/1.5045576
- 968 Thornton, A. R., Gray, J. M. N. T., & Hogg, A. J. (2006). A three-phase mixture theory for
969 particle size segregation in shallow granular free-surface flows. *Journal of Fluid*
970 *Mechanics*, *550*, 1–25, doi:10.1017/S0022112005007676
- 971 Tripathi, A., & Khakhar, D. V. (2011). Rheology of binary granular mixtures in the dense flow
972 regime. *Physics of Fluids*, *23*(11), doi:10.1063/1.3653276
- 973 Tripathi, A., & Khakhar, D. V. (2013). Density difference-driven segregation in a dense granular
974 flow. *Journal of Fluid Mechanics*, *717*, 643–669, doi:10.1017/jfm.2012.603
- 975 Trulsson, M., Andreotti, B., & Claudin, P. (2012). Transition from the viscous to inertial regime

- 976 in dense suspensions. *Physical Review Letters*, 109(11), 1–5,
977 doi:10.1103/PhysRevLett.109.118305
- 978 Tunuguntla, D. R., Bokhove, O., & Thornton, A. R. (2014). A mixture theory for size and
979 density segregation in shallow granular free-surface flows. *Journal of Fluid Mechanics*,
980 749(2014), 99–112, doi:10.1017/jfm.2014.223
- 981 Tunuguntla, Deepak R., Weinhart, T., & Thornton, A. R. (2016). Comparing and contrasting
982 size-based particle segregation models. *Computational Particle Mechanics*,
983 doi:10.1007/s40571-016-0136-1
- 984 Umbanhowar, P. B., Lueptow, R. M., & Ottino, J. M. (2019). Modeling Segregation in Granular
985 Flows. *Annual Review of Chemical and Biomolecular Engineering*, 10, 1–25,
986 doi:10.1146/annurev-chembioeng-060718-030122
- 987 van der Vaart, K., Lantman, M. P. V. S., Weinhart, T., Luding, S., Ancy, C., & Thornton, A. R.
988 (2018). Segregation of large particles in dense granular flows suggests a granular Saffman
989 effect. *Physical Review Fluids*, 074303, 1–12. doi:10.1103/PhysRevFluids.3.074303
- 990 van der Vaart, K., Gajjar, P., Epely-Chauvin, G., Andreini, N., Gray, J. M. N. T., & Ancy, C.
991 (2015). Underlying Asymmetry within Particle Size Segregation. *Physical Review Letters*,
992 114(23), 1–5. <https://doi.org/10.1103/PhysRevLett.114.238001>
- 993 van der Vaart, K., Thornton, A. R., Johnson, C. G., Weinhart, T., Jing, L., Gajjar, P., ... Ancy,
994 C. (2018). Breaking size-segregation waves and mobility feedback in dense granular
995 avalanches. *Granular Matter*, 20(3). doi:10.1007/s10035-018-0818-x
- 996 Weatherley, D., Hancock, W., Boros, V., & Abe, S. (2014). ESyS-Particle Tutorial and User's
997 Guide Version 2.3.1, 1–152.
- 998 Weinhart, T, Luding, S., & Thornton, A. R. (2013). From Discrete Particles to Continuum Fields
999 in Mixtures, 1202, doi:10.1063/1.4812153
- 1000 Weinhart, T., & Thornton, A. R. (2017). Comparing and contrasting size-based particle
1001 segregation models: applying coarse-graining to perfectly bidisperse systems.
1002 *Computational Particle Mechanics*, 4(4), 387–405, doi:10.1007/s40571-016-0136-1
- 1003 Yohannes, B., & Hill, K. M. (2010). Rheology of dense granular mixtures: Particle-size
1004 distributions, boundary conditions, and collisional time scales. *Physical Review E*, 82(6), 1–
1005 9, doi:10.1103/PhysRevE.82.061301
- 1006 Zanuttigh, B., & Ghilardi, P. (2010). Segregation process of water-granular mixtures released
1007 down a steep chute. *Journal of Hydrology*, 391(1–2), 175–187,
1008 doi:10.1016/j.jhydrol.2010.07.016
- 1009 Zhao, T., Houlsby, G. T., & Utili, S. (2014). Investigation of granular batch sedimentation via
1010 DEM–CFD coupling. *Granular Matter*, 16(6), 921–932. doi:10.1007/s10035-014-0534-0

- 1011 Zhao, Tao. (2017). Coupled DEM-CFD analyses of landslide-induced debris flows.
- 1012 Zhao, Y., Xiao, H., Umbanhowar, P. B., & Lueptow, R. M. (2018). Simulation and modeling of
1013 segregating rods in quasi-2D bounded heap flow, *64*(5). <https://doi.org/10.1002/aic.16035>
- 1014 Zhou, G. G. D., Li, S., Song, D., Choi, C. E., & Chen, X. (2019). Depositional mechanisms and
1015 morphology of debris flow: physical modelling. *Landslides*, *16*(2), 315–332,
1016 doi:10.1007/s10346-018-1095-9
- 1017 Zhou, G. G. D., & Ng, C. W. W. (2010). Numerical investigation of reverse segregation in debris
1018 flows by DEM. *Granular Matter*, *12*(5), 507–516, doi:10.1007/s10035-010-0209-4
- 1019 Zhou, G. G. D., & Sun, Q. C. (2017). Study of Pore Fluid Effect on the Mobility of Granular
1020 Debris Flows. In *Powders and Grains*, 09046, 1–4.
- 1021
- 1022